

Linking Holocene East Asian monsoon variability to solar forcing and ENSO activity: Multi-proxy evidence from a peatland in Northeastern China

The Holocene
2021, Vol. 31(6) 966–982
© The Author(s) 2021
Article reuse guidelines:
sagepub.com/journals-permissions
DOI: 10.1177/0959683621994662
journals.sagepub.com/home/hol
 SAGE

Nannan Li,^{1,2,3} Arash Sharifi,⁴ Frank M Chambers,⁵ Yong Ge,⁶
Nathalie Dubois,^{7,8} Guizai Gao,^{1,3} Dehui Li,⁹ Lidan Liu,¹⁰
Hongyan Liu,¹¹ Jiangyong Wang,^{1,3} Honghao Niu,^{1,3} Meng Meng,^{1,3}
Ying Liu,^{1,3} Guihua Zhang^{1,3} and Dongmei Jie^{1,3,12}

Abstract

High-resolution proxy-based paleoenvironmental records derived from peatlands provide important insights into climate changes over centennial to millennial timescales. In this study, we present a composite climatic index (CCI) for the Hani peatland from northeastern China, based on an innovative combination of pollen-spore, phytolith, and grain size data. We use the CCI to reconstruct variations of the East Asian summer monsoon (EASM) intensity during the Holocene. This is accomplished with complete ensemble empirical mode decomposition (CEEMD), REDFIT, and cross-wavelet coherency analysis to reveal the periodicities (frequencies) of the multi-proxy derived CCI sequences and to assess potential external forcing of the EASM. The results showed that periodicities of ca. 300–350, 475, 600, 1075, and 1875 years were present in the Hani CCI sequence. Those periodicities are consistent with previously published periodicities in East Asia, indicating they are a product of external climate controls over an extensive region, rather than random variations caused by peatland-specific factors. Cross-wavelet coherency analysis between the decomposed CCI components and past solar activity reconstructions suggests that variations of solar irradiation are most likely responsible for the cyclic characteristics at 500-year frequency. We propose a conceptual model to interpret how the sun regulates the monsoon climate via coupling with oceanic and atmospheric circulations. It seems that slight solar irradiation changes can be amplified by coupling with ENSO events, which result in a significant impact on the regional climate in the East Asian monsoon area.

Keywords

climate cycle, East Asian summer monsoon, Holocene, Northeastern China, peatlands, solar irradiation

Received 24 October 2020; revised manuscript accepted 5 January 2021

Introduction

Recognition of the characteristics and forcing of natural climate cycles on different timescales is critical for understanding the magnitude and rapidity of climate change. The cyclic nature of the Earth's climate during the last glacial period has been suggested to

be paced by a ~1500-year periodicity (Dansgaard et al., 1993), but the origin of this pacing during the Holocene remains controversial. Bond et al. (1997, 2001) attributed the Holocene millennial climate cycle to solar irradiation. However, owing to the lack of a corresponding ~1500-year cycle in past solar activity reconstructions, the mechanism of Holocene millennial variability has stimulated a

¹Key Laboratory of Geographical Processes and Ecological Security in Changbai Mountains, Ministry of Education, China

²State Key Laboratory of Marine Environmental Science, College of Ocean and Earth Sciences, Xiamen University, China

³Institute for Peat and Mire Research, State Environmental Protection Key Laboratory of Wetland Ecology and Vegetation Restoration, Northeast Normal University, China

⁴Neptune Isotope Laboratory (NIL), Department of Marine Geosciences, Rosenstiel School of Marine and Atmospheric Science, University of Miami, USA

⁵Centre for Environmental Change and Quaternary Research, School of Natural and Social Sciences, University of Gloucestershire, UK

⁶Department of Archaeology and Anthropology, School of Humanities, University of Chinese Academy of Sciences, China

⁷Surface Waters – Research and Management, Eawag, Swiss Federal Institute of Aquatic Science and Technology, Switzerland

⁸Department of Earth Sciences, ETH Zürich, Switzerland

⁹College of Resources and Environment Sciences, Hebei Normal University, China

¹⁰College of Resource and Environment Science, Hunan Normal University, China

¹¹School of Resources Environment and Tourism, Anyang Normal University, China

¹²Key Laboratory of Vegetation Ecology, Ministry of Education, China

Corresponding author:

Dongmei Jie, School of Geographical Sciences, Northeast Normal University, No. 5268, Renmin Street, Changchun 130024, Jilin, P.R. China.

Email: jiedongmei@nenu.edu.cn

substantial debate (e.g. Braun et al., 2005; Darby et al., 2012; Debret et al., 2007; Obrochta et al., 2012; Ojala et al., 2015; Wanner and Bütikofer, 2008). Over the last decade, the use of spectrum analysis on proxy-based paleoclimate reconstructions has produced increasing evidence to confirm the existence of Holocene centennial- to millennial climate cycles (e.g. Obrochta et al., 2012; Ojala et al., 2015; Soon et al., 2014; Stebich et al., 2015; Swindles et al., 2012; Xu et al., 2014, 2019, 2020). However, until now, an agreed theory for these Holocene periodic oscillations and their potential forcing is still lacking. Furthermore, most of the existing records have focused largely on marine sediments (e.g. Bianchi and McCave, 1999; Bond et al., 2001), ice-cores (e.g. Stuiver et al., 1995) and stalagmites (e.g. Jo et al., 2017; Wang et al., 2005a) with uneven spatial distributions; few of them were from lakes or peatlands, which are directly coupled to the atmosphere and can provide continuous records to evaluate the potential external forcing for continental climate changes (Swindles et al., 2012).

The East Asian monsoon (EAM) is an important component of the global climate system (Wang et al., 2017). Monsoon rainfall in eastern Asia benefits nearly one-quarter of the world's population. Past East Asian monsoon variations have been investigated at different time scales using loess (e.g. Beck et al., 2018), stalagmites (e.g. Wang et al., 2005a) and lacustrine (e.g. Chen et al., 2015) sediments, which have significantly improved understanding of regional climate changes in the monsoon area. The forcing and regulation mechanism of the East Asian Summer Monsoon (EASM) variation, however, is still controversial and has been attributed variously to orbital insolation changes (Wang et al., 2001, 2005a), low-latitude inter-hemispheric insolation gradients (Beck et al., 2018) and global ice volume variations (Stevens et al., 2018).

Table 1 lists papers published since 1999 reporting cyclic characters of East Asian monsoon climates reconstructed from various archives using a range of proxies. It demonstrates the existence of periodic cycles in the paleoclimate reconstructions of East Asia; solar insolation variations and global deep-water flow dynamics are the most reported pacemakers thought responsible for the periodic climate oscillations (Table 1). According to frequency statistics on currently reported periodicities in East Asia, as shown in Figure 1, the 200-year and 350-year cycle, as well as 500-year cycle, are the most commonly reported in the listed papers (Table 1). Although evidence for millennial- and centennial-scale climate cycles across East Asia is increasing, one single, agreed theory explaining the forcing factor and possible mechanism has not yet emerged (e.g. Beck et al., 2018; Jo et al., 2017; Lu et al., 2019; Stebich et al., 2015; Stevens et al., 2018; Wang et al., 2001, 2005a, 2005b, 2017; Xu et al., 2014, 2019, 2020). Therefore, additional terrestrial records from the EAM region are still required to establish a credible hypothesis regarding the cyclic characteristics of EASM activity. Meanwhile, the publication of high-resolution Holocene paleoclimate reconstructions during recent decades requires a synthetic review (even recalculation) of current trends in Holocene climate cycles and their potential forcing mechanisms for the EAM region.

Peatlands provide an important archive of Holocene environmental change. The moist environments in which peat forms encourage the growth of vascular plants and retard decomposition of their remains to produce organic-rich material that can be used for high-resolution paleoenvironmental reconstructions (Barber and Langdon, 2007; Chambers and Charman, 2004; Dise, 2009). Benefiting from a wide range of climate proxies and accurate radiocarbon dating, peatlands hold great potential for research into cyclical characters of Holocene climate (Chambers and Charman, 2004; Chambers et al., 2012). Northeastern China is one of the most important peat distribution regions of the world (Chai, 1990). Up to now, using a wide range of proxies, several Holocene paleoclimate reconstructions have been carried out on peat deposits in the Changbai Mountains, northeastern China (see Li et al., 2017;

Zhang et al., 2019 and references therein). These pioneering studies confirm that northeastern China, located near the northern margin of the EAM, is sensitive to monsoonal climate variations. However, few of them have focused on the cyclical characteristics of Holocene climate and on the physical mechanism that modulated the intensity of the EASM (Stebich et al., 2015; Wu et al., 2019; Xu et al., 2014, 2019, 2020). Accompanied with an improved radiocarbon-dated chronology, here we present a new pollen-spore, phytolith, and grain size dataset from Hani peatland in northeastern China. Using principal component analysis (PCA), a composite climatic index based on pollen, phytolith, and grain size data, was defined and calculated to reconstruct Holocene paleoclimatic changes recorded in peats. We further conducted spectrum and wavelet analysis on the composite climate indices to reveal the potential forcing and the mechanism that regulates EASM climate change in East Asia.

Regional setting

Hani (HN) is a minerotrophic and ombrotrophic peatland, located in the Longgang Volcanic Field, northeastern China, which is one of the most active volcanic areas in China (Liu, 1988). The intense Cenozoic volcanic activities in this region provided a geological basis for the development of peatlands. The Hani peatland was formed in a paleo-lake basin that was dammed by volcanic ejecta in the Late Pleistocene (Qiao, 1993).

The modern climate of the study area is controlled by the EAM, which shows strong seasonal variability (Chao and Chen, 2001). In the winter, cold and dry north-westerly winds initiated from the interior of the Eurasian landmass blow strongly toward north China, while the summers are dominated by warm and humid air, transported by southerly winds from the Indian Ocean and the Pacific (Figure 2a and c). The main period of regional rainfall is concentrated from June to September, which accounts for more than 70% of the annual precipitation. The mean annual temperature of the Changbai Mountains ranges from -7.3°C to 4.8°C , while the average annual rainfall ranges from 700 to 1400 mm (Wang, 1989). The landform type in the Changbai Mountains is diverse and the dominant soil in the study region is dark brown forest soil, but with meadow soils in valleys and albic soil on high tableland. The natural vegetation in this area is temperate conifer–broadleaf mixed-forest.

Naturally, the conifer–broadleaf mixed-forest is dominated by a variety of arboreal species, including *Pinus koraiensis*, *Picea jezoensis*, *P. koraiensis*, *Abies nephrolepis*, *Larix olgensis*, *Tilia amurensis*, *T. mandshurica*, *Betula platyphylla*, *Quercus mongolica*, *Acer pictum*, *Juglans mandshurica*, *Populus davidiana*, *Ulmus pumila*, *Fraxinus mandshurica* and *Phellodendron amurense* (Wu, 1980). Since the 1970s, the regional vegetation surrounding the Hani peatlands has undergone considerable modification by anthropogenic woodcutting, resulting in extensive secondary succession of regional vegetation. The local vegetation of the Hani peatland is covered by shrubs and wetland species (Schröder et al., 2007). The shrub layer is mainly composed of *Larix olgensis*, *Betula fruticosa*, *Vaccinium uliginosum*, *Ledum palustre*, and *Chamaedaphne calyculata*. The field layer comprises *Carex* spp., *Sphagnum magellanicum*, *S. fuscum*, *Equisetum hyemale*, *Juncus effusus*, *Menyanthes trifoliata*, *Comarum palustre*, *Sanguisorba tenuifolia*, *Phragmites australis*, etc.

Materials and methods

Peat recovery and data sources

A 350 cm peat core from Hani ($42^{\circ}13'31.1''\text{N}$, $126^{\circ}30'14.7''\text{E}$, 890 m a.s.l.) peatland was sampled in the summer of 2009 (Figure 2b), using an Eijkelpamp peat sampler. The lithologic stratification and radiocarbon dating layers are shown in Figure S1. The

Table 1. Reported Holocene climate cycles, and their claimed potential forcing mechanism, from various records and proxies in monsoonal Asia.

Location	Materials	Proxies	Periods (years)	Possible mechanism	Reference
South China Sea	Marine sediments	$\delta^{18}\text{O}$ of foraminifera	84, 102, 775	Global thermohaline circulation in the ocean or short-term changes in solar activity	Wang et al. (1999)
Okinawa Trough	Marine sediments	Foraminifera	700–800, ~1500	Climate tele-connections to Bond cycles	Jian et al. (2000)
Lake Huguangyan	Lake sediments	Dry density	220, 250, 490, 1140, 2930	Global thermohaline circulation and global water cycle	Liu et al. (2000)
Jinchuan	Peat	α -Cellulose $\delta^{18}\text{O}$	86, 93, 101, 110, 127, 132, 140, 155, 207, 245, 311, 590, 820, 1046	Solar irradiation variations	Hong et al. (2000)
South China Sea	Marine sediments	Pollen	780, 1500, 2900, 7100	Unclear	Luo and Sun (2005)
Lake Qinghai	Lake sediments	Redness	123, 163, 200, 293	Solar irradiation	Ji et al. (2005)
Hani	Peat	Pollen	300, 500, 700, 1100	Solar irradiation, thermohaline circulation and deep-sea water cycle (?)	Yu et al. (2008)
Dongge Cave	Speleothem	$\delta^{18}\text{O}$	23, 28, 43, 65, 88, 120, 153, 212, 568, 930, 2040	Solar irradiation variations	Liu et al. (2012)
Lake Xiaolongwan	Lake sediments	Pollen	~500	Solar irradiation variations	Xu et al. (2014)
Lake Xiaolongwan	Lake sediments	Biomarker	87–89, 140–150, 210, 1020–1050, 1750–2041	Solar irradiation, sea surface temperature variations	Chu et al. (2014)
Lake Sihailongwan	Lake sediments	Pollen	500–600	Variations in the coupled Atmospheric-Pacific Ocean system	Stebich et al. (2015)
Dajuhu	Peat	Elements	188, 204, 316, 360, 1480	Solar forcing and North Atlantic climate changes	Li et al. (2016)
Baeg-nyong Cave	Speleothem	$\delta^{18}\text{O}$	41, 48, 63, 112, 182, 335, 1089	Solar irradiation changes and ocean-ice sheet dynamics	Jo et al. (2017)
Lake Gonghai	Lake sediments	Pollen	160, 400, 684, 2162	Solar activity and Atlantic Multidecadal Oscillation	Zhang et al. (2017)
Heshang Cave	Speleothem	Magnetic minerals	~500, 800, 2000	Periodic solar activity and ENSO variation	Zhu et al. (2017)
Lake Moon	Lake sediments	Pollen	~500	Caused by solar activity and amplified by ocean circulation ENSO	Wu et al. (2019)
South China Sea	Marine sediments	K/Al ratio	110, 132, 158, 405	Triggered by solar activity	Huang et al. (2019)
Lake Nakaumi	Ostracod shells	$\delta^{18}\text{O}$	125, 206, 246	Solar activity	Yamada et al. (2019)
Dajuhu	Peat	Phytoliths	~280, ~1000	ENSO variation	Liu et al. (2019)

core was sub-sampled at 1-cm intervals, resulting in 350 sub-samples, and then analyzed every 2-cm intervals. To overcome the site-specific effects of single core investigations, in addition to our dataset, several quantitatively reconstructed paleoclimate and paleovegetation sequences were used and analyzed for periodicities. Those reference sites were selected based on the following criteria: (1) sites that are located in the same or adjacent bioclimatic region; (2) with a minimum of eight dating controls for the Holocene; (3) with high sampling resolution better than 100-year per sample; and (4) a continuous record covering most of the Holocene without obvious sedimentary hiatus. Those sequences were Holocene *Pinus* and *Quercus* pollen percentages from Lake Moon (Wu et al., 2019), pollen-derived Holocene mean July temperature (Mtw) and mean annual precipitation (Pann) sequences from Lake Sihailongwan (Stebich et al., 2015), Holocene *Quercus* pollen percentages from Lake Xiaolongwan (Xu et al., 2019), pollen-derived mean annual precipitation (Pann) from Lake Daihai (Ding et al., 2018; Xiao et al., 2004) and Lake

Gonghai (Ding et al., 2018; Xu et al., 2017). The locations of those sites are displayed in Figure 2. Meanwhile, the IntCal13 $\Delta^{14}\text{C}$ dataset, the deviation of the atmospheric $^{14}\text{C}/^{12}\text{C}$ ratio from a standard value (Liu et al., 2012; Reimer et al., 2013; Steinhilber et al., 2012), is used as a proxy for past solar activity.

Radiocarbon dating and age-depth modeling

We present a new “age-depth” model for the Hani peat core in addition to our previously published chronology in Li et al. (2017). Five new radiocarbon dates were added to the profile to make a better age control to facilitate spectral analysis. For radiocarbon dating preparation, samples were treated with 1M HCl (70°C, 12h) after the removal of any visible roots, washed free from acid with Milli-Q water, then dried (65°C) and homogenized (Piotrowska et al., 2011). The organic carbon in a pre-treated sample was converted into CO_2 by combustion with CuO in a sealed quartz tube; after purification, the gas was reduced into graphite by Fe/Zn reduction (Xu et al., 2007) at Northeast Normal University. The graphite was then analyzed for ^{14}C activity with Accelerator Mass Spectrometry (AMS) at Guangzhou Institute of Geochemistry, Chinese Academy of Sciences (GIGCAS) (Zhu et al., 2015). All ages are reported in conventional age before present (year BP) and calibrated into calendar years with the IntCal20 calibration curve (Reimer et al., 2020) using the CALIB 8.10 program and expressed as cal. yr BP with 2σ ranges (Stuiver and Reimer, 1993). The chronologies were estimated with the “rbacon” package (v 2.5.0) in R (Blaauw and Christen, 2011).

Laboratory methods

Pollen-spore samples at 10cm intervals from the Hani section were prepared for analysis. The samples were treated with KOH, HCl, HF, and a hot acetylation mixture. Sample residues were preserved in glycerine and analyzed by Leitz Orthoplan microscope at 600 \times magnification. Pollen-spore analysis of the Hani peat core was conducted at Jilin University, China.

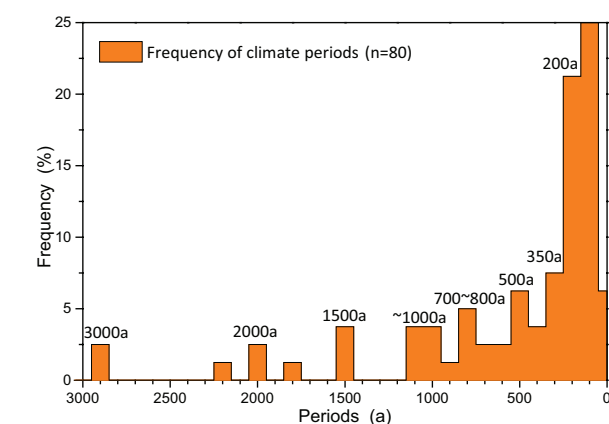


Figure 1. Frequency counts ($n=80$) on published Holocene millennial and centennial climate cycles in East Asia.

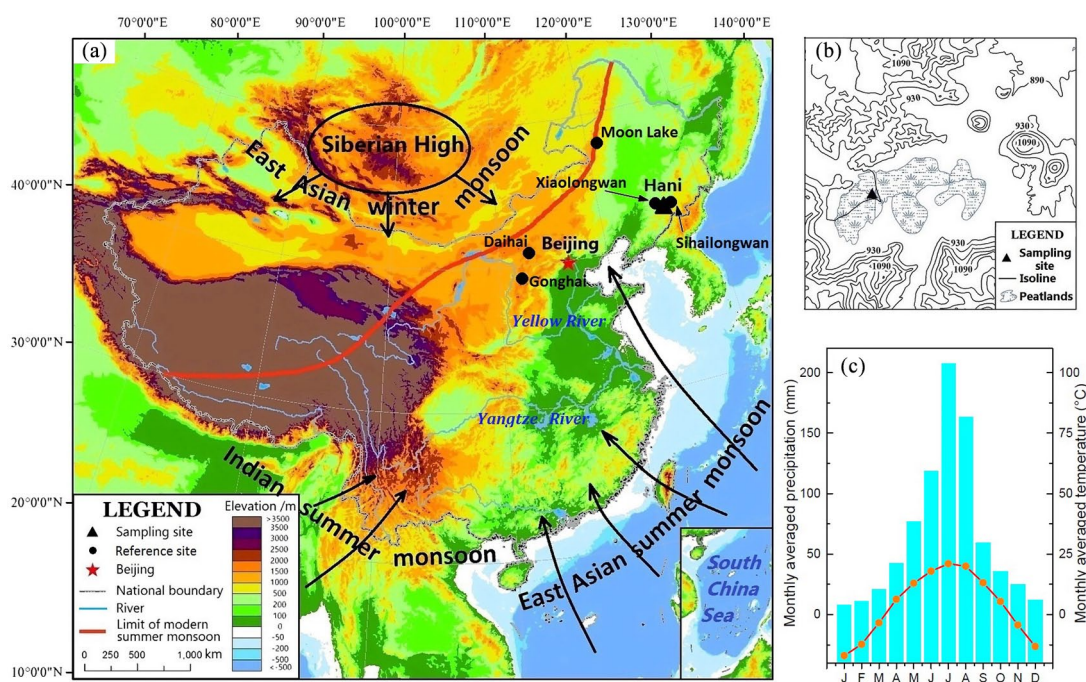


Figure 2. Investigation area and the locations of sampling and comparison sites in East Asia. (a) East Asian monsoon area and surroundings with ETOPO1 1 arc-minute global relief model (Amante and Eakins, 2009) and main regional atmospheric circulations (black arrows). (b) Hani peatlands and geographical setting. (c) Climatic pattern for the sampling area.

Diagrams show average monthly temperature and precipitation of Jingyu station from 1981 to 2010.

Phytoliths were extracted from approximately 0.5 g crushed dried peat samples using 10% HCl to remove carbonates, followed by using 65% HNO₃ in water-bath heating (80°C) to remove organics. The phytoliths were extracted from the residues using density separation (the density of heavy liquid is 2.35 g/cm³, ZnBr₂). Phytolith counting was conducted under a Motic optical microscope at 600× magnification until about 300 phytolith grains were identified.

For grain size measurements, all samples were pretreated in a muffle furnace (550°C) for 4 h to remove organic matter, 10% hydrochloric acid (HCl) to remove carbonates and with 10 mL 0.05 mol/L sodium hexametaphosphate ((NaPO₃)₆) to facilitate dispersion. The grain size distribution was determined with a MICROTRAC S3500 particle analyzer at Northeast Normal University, China.

The loss-on-ignition (LOI) method was used to determine the total organic carbon content of the peat samples. For analysis, each sample of approximately 1 g oven-dried (105°C) peat was weighed in a crucible. The crucible was then placed in a muffle furnace (SX-8-10, Taisite, China) and combusted for 12 h at 500°C. After combustion, the sample was cooled in desiccators to room temperature and weighed again. All samples were weighed using a 0.1 mg analytical balance (BSA124S-CW, Sartorius, Germany). The TOC content was calculated as the weight loss at 500°C according to equations in Li et al. (2020).

Numerical methods

Ordination correspondence analysis and proxy classification. The relationships between the pollen-spore, phytolith assemblages and grain size parameters were analyzed by correspondence analysis. A pre-analysis (detrended correspondence analysis, DCA) was required to determine whether a redundancy analysis (RDA) or principal component analysis (PCA) technique should be used for proxy classification (grouping). The analysis was processed using the program CANOCO version 4.5 (ter Braak and Šmilauer, 2002).

Principal component analysis and past EASM intensity reconstruction. In a correspondence diagram, proxy taxa (for instance, pollen vs phytolith and grain-size vs phytolith in this study) are classified into contrasting indicative groups along different directions of the RDA (or PCA) axis, indicating diametrically different climate/environment implications for each group. Based on the proxy correspondence diagram, the phytolith, pollen-spore assemblages, and grain size parameters were then classified into two indicative groups: a strong EASM-indicated group and a weak EASM-indicated group.

We then undertook PCA to extract principal components that explain the variations of the strong/weak EASM-indicated proxy dataset. Before PCA, the raw data of pollen, phytolith, and grain-size were normalized to a sequence with a mean value of zero and standard deviation of one. All the strong EASM-indicated (or weak EASM-indicated) proxies (data from pollen, phytolith, and grain-size) were put together and processed by PCA to calculate the strong EASM (or weak EASM) loading for each principal component. The strong/weak EASM scores were defined as the total principal component scores, which were calculated as the sum of weighted principal factor-scores (loadings) for strong/weak EASM groups. Then, a composite climate index (CCI), based on the multiple proxies, was calculated as the sum of the strong EASM and weak EASM scores for each sample. The PCA was performed with SPSS 19.0 software (Statistical Package for Social Sciences, Chicago, IL, USA).

Complete ensemble empirical mode decomposition and spectrum analysis. To identify the major periodicities within the time series, the CCI series for the Hani peat core was processed using the

least-squares best-fit line and was linearly interpolated from the original data at constant 90-year steps using the built-in MATLAB command, to provide an equally spaced time series. This was because the 90-year steps closely approximate the average temporal sampling resolution of the Hani CCI time series. Subsequently, the dataset was decomposed into its major components using the complete ensemble empirical mode decomposition (CEEMD) approach (Sharifi et al., 2015; Torres et al., 2011). Wavelet power spectrum analyses were performed on each individual component using the Morlet wave (Torrence and Compo, 1998) with a modified MATLAB script. Notable periodicities with global power spectra >1σ confidence level were considered significant according to the wavelet power spectra of each component.

In addition to CEEMD, spectral analyses were performed using REDFIT 3.8e (Schulz and Mudelsee, 2002) on the original unevenly spaced CCI data. The program involves the Lomb-Scargle Fourier transform to overcome unequal time intervals. A first-order autoregressive (AR1) parameter was generated from the dataset and presented in the frequency domain to test whether spectral peaks are significant against the red-noise background generated from a first-order autoregressive process (as the null hypothesis).

Considering the aim of looking for Holocene climate cyclic characteristics and their potential mechanism, here we only processed the Holocene CCI data (since 11,700 cal. yr BP) for spectral and wavelet analyses.

Results

Chronologies

Radiocarbon dating results and calibrated ages are listed in Table 2. The calibrated ages for the Hani peatland reflected the sample stratigraphic order within dating errors, without obvious inverted outliers (Table 2). Bacon-estimated chronologies suggest that the sequence recorded a continuous paleovegetation and paleoclimate evolution surrounding the Hani peatland from ca. 16,000 cal. yr BP to present (Figure 3). Meanwhile, the newly established age-depth model is almost identical with the previously published chronology in Li et al. (2017), underlining the reliability of our dating and chronology estimation methods.

Microfossil assemblages and grain size data

Pollen-spore assemblages and regional vegetation development. Starting with the deglaciation period, the pollen diagram of Hani peatland covers the last 16,000 cal. yr BP (Figure S2). The pollen-spore spectra were dominated by Cyperaceae and various tree pollen types (Figure S2), indicating a forest swamp environment. The pollen sequence was visually divided into five pollen assemblage zones based on major changes in pollen assemblages.

Zone I (346–298 cm; 16,000–12,200 cal. yr BP) is exclusively dominated by *Abies*, *Picea*, and Cyperaceae where the abundances of broadleaf tree pollen are the lowest in the peat core, suggesting a boreal forest ecosystem surrounding the peatland.

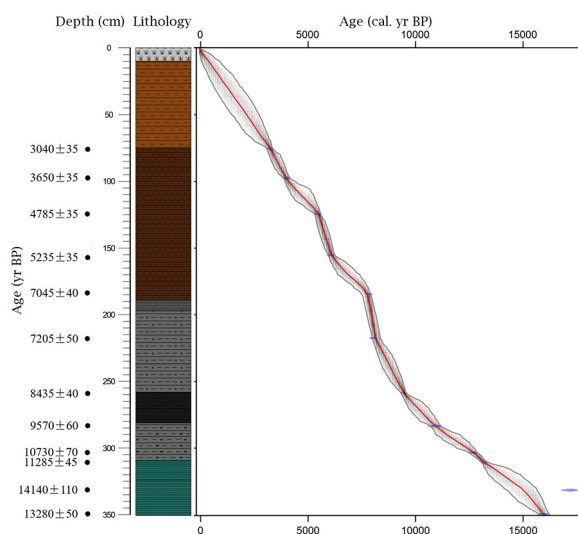
Zone II (298–234 cm; 12,200–8700 cal. yr BP) is marked by increasing abundances of broad-leaved tree pollen and decreased Cyperaceae pollen. The Late-glacial climatic amelioration is palynologically indicated by the obvious increases in more thermophilous taxa, such as *Juglans*, *Quercus*, and *Ulmus*, revealing a shift in the regional vegetation composition to temperate broadleaf deciduous forests. Other temperate broadleaf deciduous trees, such as *Carpinus* and *Corylus*, become slightly more abundant. Boreal conifers, however, almost disappear from the study region as indicated by only scattered occurrences of conifer pollen (Figure S2).

Zone III (234–128 cm; 8700–5600 cal. yr BP): *Juglans*, *Quercus*, and *Ulmus* continue to dominate the pollen spectra. The mid-Holocene climate optimum is marked by rapid increases of

Table 2. Accelerator mass spectrometry (AMS) radiocarbon (^{14}C) dates of samples from the Hani peat core.

Depth (cm)	Lab. code	Material	AMS ^{14}C BP	Uncertainty	2 σ -Range cal. BP	Median age, cal. BP
75–76	BA091607	Bulk organic matter	3040	35	3151–3360	3248
97–98	NENUR10562*	Bulk organic matter	3650	35	3874–4088	3971
124–125	BA091608	Bulk organic matter	4785	35	5335–5591	5523
155–156	BA091609	Bulk organic matter	5235	35	5915–6176	5986
184–185	BA091610	Bulk organic matter	7045	40	7787–7962	7879
217–218	NENUR10563*	Bulk organic matter	7205	50	7935–8169	8009
258–259	BA091613	Bulk organic matter	8435	40	9323–9533	9470
283–284	NENUR10565*	Bulk organic matter	9570	60	10,708–11,157	10,928
303–304	NENUR10566*	Bulk organic matter	10,730	70	12,505–12,820	12,717
310–311	BA091614	Bulk organic matter	11,285	45	13,098–13,295	13,173
331–332	NENUR10567*	Bulk organic matter	14,140	110	16,914–17,460	17,201
349–350	BA091615	Bulk organic matter	13,280	50	15,772–16,141	15,954

*The graphite was prepared at Northeast Normal University and analyzed at Guangzhou Institute of Geochemistry, Chinese Academy of Sciences (GIGCAS).

**Figure 3.** “rbacon” estimated age-depth model for Hani peat core. The best estimates for calibrated age are shown in red. The upper and lower estimates are shown in gray.

broadleaved trees with maximum pollen percentage values during 8000–6000 cal. yr BP. Interestingly, the representation of Cyperaceae, which decreased during stage II, increases again since about 8200 cal. yr BP, clearly reflecting a trend toward relatively warm and moist climate conditions during the mid-Holocene.

Zone IV (128–64 cm; 5600–2700 cal. yr BP) is characterized by sharply increased values for *Pinus* pollen whose average percentage is more than 30% (Figure S2). The broadleaved trees, such as *Juglans*, *Quercus*, *Ulmus*, start to decrease and gradually no longer dominate the pollen spectra. This shift in vegetation cover documents a substantial spread of *Pinus* species at ca. 5300 cal. yr BP, possibly indicating that *Pinus* is becoming a common component of the regional vegetation. In the ground layer, *Artemisia*, which is tolerant of dryness, slightly increases at this stage, which suggests that the climate is becoming drier.

Zone V (64–0 cm; 2700 cal. yr BP to the present): similar to Zone IV, the regional vegetation is dominated by various conifers (e.g. as shown by pollen of *Pinus*, *Abies*, and *Picea*). Broadleaf tree pollen types significantly decrease during the late-Holocene while the Cyperaceae pollen slightly increases (Figure S2). *Pinus* contributes more than 50% of arboreal pollen while *Picea* is present up to ~6%. The regional landscape gradually evolves into the modern temperate needle-leaf and broadleaf mixed forest.

Phytolith assemblages. The peaty samples yield abundant phytolith types attributed to different species (Figure S3). The phytolith spectra are dominated by various elongates, rondel, trapeziform crenate, lanceolate, and bilobate phytoliths (Figure S3). The CONISS identified five first-order phytolith stratigraphic zones in the peat core. Two additional second-order subzones (Ia and Ib) were identified within phytolith Zone I.

Phytolith Zone I (346–286 cm; 16,000–11,000 cal. yr BP) covers most of the late-glacial period, during which the dominant phytolith types and contents were significantly different from those in the Holocene (Figure S3). Zone Ia (346–308 cm; 16,000–13,000 cal. yr BP) is dominated by elongate, trapeziform, and lanceolate phytoliths. Elongates contribute nearly 50% of the total assemblage. Bilobate phytoliths, which are more abundant in semi-humid regions (Lu et al., 2006), have the lowest percentages in the core (Figure S3). In Zone Ib (308–286 cm; 13,000–11,100 cal. yr BP), trapeziform crenate phytoliths significantly increase to the highest values in the core (Figure S3), indicating the regional climate becomes drier (Lu et al., 2006). Elongate, trapeziform, and lanceolate phytoliths continue to dominate the phytolith spectra; however, compared with Zone Ia, rondel slightly increase while the elongate and square decrease within this interval.

The phytolith assemblage of Zone II (286–214 cm; 11,100–8200 cal. yr BP) clearly reflected the early-Holocene climate amelioration: trapeziform crenate and lanceolate significantly decreased and no longer dominate the phytolith spectra. The bilobate and square phytoliths, which have higher abundances in wetter climates (Lu et al., 2006), increased during this stage.

Zone III (214–168 cm; 8200–6800 cal. yr BP) is marked by an increase in rondel, bilobate, and square phytoliths, revealing a favorable climate that may correspond to the mid-Holocene optimum. Elongate phytoliths decrease while blocky phytoliths slightly increase (Figure S3).

In Zone IV (168–64 cm; 6800–2700 cal. yr BP), the rondel phytoliths continue to increase, attaining the highest percentages of the core (21% on average). Trapeziform crenate increase whereas the square types significantly decrease. Considering the modern phytolith-climate calibrations (Gao et al., 2018; Lu et al., 2006), the phytolith assemblage variations during this stage seem mainly caused by mid- to late-Holocene climate deterioration.

Zone V (64–0 cm; 2700 cal. yr BP to the present) is characterized by the increase in elongate phytoliths and decrease in the rondel types. Trapeziform crenate continue to increase but not to values reached during the late-glacial age. The bilobate and the square types, which are common in warm and wet climate conditions (Lu et al., 2006), present lowered abundances within this interval, indicating cool and/or dry climate conditions in the late-Holocene.

Grain-size characters of Hani peat. The grain size parameters of the Hani peat core displayed significant variations, which could be divided into five different stages.

Zone I (346–238 cm; 16,000–8800 cal. yr BP) is characterized by high percentages of fine-grained clasts in peats. The peaty sediments are mainly composed of silt (78% on average) and clay (9% on average), with the mean grain-size of the sediments varying from 20 to 40 μm . Zone Ia (346–286 cm; 16,000–11,100 cal. yr BP) covers the late-glacial period, during which the regional climate is cold and dry; wind-blown fine components contribute the fine-grained layers of the peat core. In addition, within this interval, the LOI is lower than in other stages and displays rapid fluctuations. The grain-size characters during the early-Holocene (Zone Ib: 286–238 cm; 11,100–8800 cal. yr BP) are similar to those in late-glacial times but show slight differences: LOI sharply increased to more than 90% at ca. 11,700 cal. yr BP; fine-grained clasts' contents started to decrease, indicating the East Asian summer monsoon-originated precipitation is increasing in the study area.

Zone II (238–198 cm; 8800–8000 cal. yr BP) is marked by a significant decrease in fine-grained components and increase in coarser clasts. The sandy component increased from 13 to 25% on average, suggesting the increase in coarse clasts came from surface flow erosion (Li et al., 2017).

Zone III (198–158 cm; 8000–6200 cal. yr BP) has the highest coarse-grained components of the peat core. The coarser component's (>37 μm) percentage is higher than 60% on average and the sandy fractions increase to 47%. Since the coarse-grained components mainly come from monsoon-induced precipitation, the higher percentages of coarse clasts may correspond to the climatic optimum during the middle Holocene (Li et al., 2017).

In Zone IV (158–90 cm; 6200–3800 cal. yr BP), the sandy components start to decrease and varied more rapidly. The fine-grained clasts (<37 μm), which were less than 40% during the mid-Holocene, now account for more than 55% of the mineral particles, suggesting a decline in the strength of the East Asian summer monsoon and increase in winter monsoon-blown fine-grained fractions.

Zone V (90–0 cm; 3800 cal. yr BP to the present) is marked by several obvious sedimentation fluctuations (Figure S4). The contents of the sandy grains peaked first at ca. 3700 cal. yr BP (more than 90%) and then decreased to about 2% at 3300 cal. yr BP. During the late-Holocene, sandy fractions gradually increase while the silty fractions in the peats gradually decreased (Figure S4).

Although the paleoclimate and paleoenvironment reconstructions from different proxy data were not identical, all the data point to a similar general trend of the regional climate evolution: during the late-glacial age, the study region was influenced by a strong East Asian winter monsoon, resulting in cold and dry regional climate conditions. Since the onset of the Holocene, the data from the Hani peat core displayed marked enhancement of the East Asian summer monsoon, suggesting a climatic shift toward a favorable temperate environment. The late-Holocene is characterized by a decreasing trend of the East Asian summer monsoon, as the regional climate gradually becomes cooler and slightly drier. The agreements among those three proxies indicate that the proxy-based reconstruction resulted from regional climate change rather than site-specific conditions. All of them could be combined to construct a multiple-proxy based composite climate index.

Composite climate index calculation

Proxies grouping. DCA results showed that the linear approach of RDA is preferable to canonical correspondence analysis (CCA) of our datasets (ter Braak and Šmilauer, 2002). All the proxy groups were separately distributed in the RDA score plot, reflecting different environmental implications. Phytoliths and pollen-spore assemblages as well as grain size parameters were generally classified

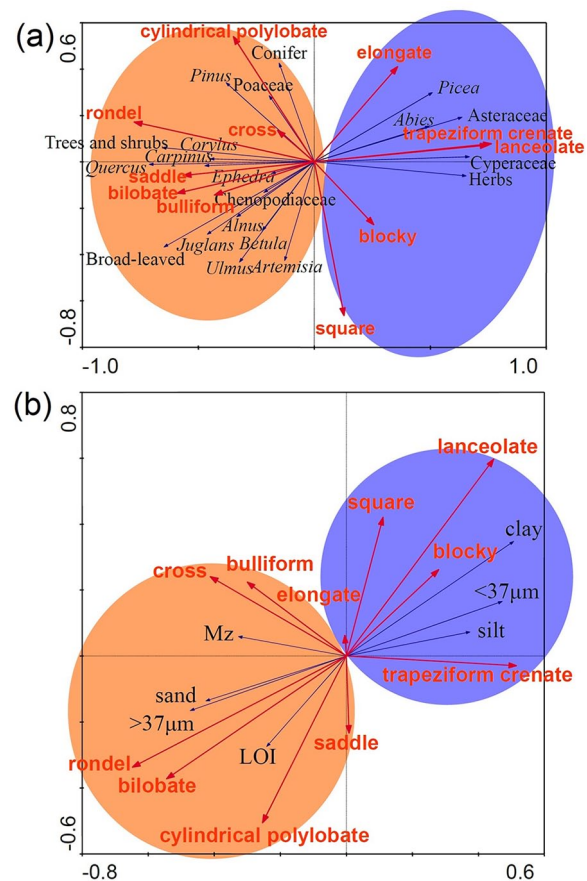


Figure 4. RDA analysis results and proxy grouping results for the Hani peat section. (a) Pollen and phytolith categories. (b) Phytolith taxa and grain size parameters. Orange: strong EASM indicated categories; blue: weak EASM indicated categories.

into two indicative groups, suggesting strong- and weak-EASM, respectively. In Figure 4, along Axis 1, phytoliths were classified into two distinct groups. Warm and humid climate-favored phytoliths, such as saddle and bilobate cross, plotted separately from elongate, lanceolate, and trapeziform crenate types, which usually occur in dry and cold climate conditions (Lu et al., 2006; Wang and Lu, 1993; Wang et al., 2003). Similarly, the pollen-spore taxa also separated into two distinct groups: thermophilous pollen and spore types (e.g. Cao et al., 2014; Chen et al., 2010; Yu et al., 2004), like broadleaf tree pollen, plotted along the minus direction of Axis 1, while coldness- and dryness-tolerant taxa, such as herbaceous plants and conifer taxa (e.g. Cao et al., 2014; Chen et al., 2010; Yu et al., 2004), plotted along the positive direction of Axis 1 (the same as phytoliths). The RDA between grain size parameters and phytolith assemblages indicated similar patterns. Strong EASM-indicated parameters, such as sand content and coarse components (>37 μm fractions) percentages, which suggest a strong summer monsoon period in northeastern China, plotted along the minus direction of Axis 1, while the weak EASM indices were in the opposite direction. In summary, RDA classified all these proxies into two major groups as they indicated different monsoon strength in northeastern China (Table 3).

PCA based composite climate index calculations. PCA extracted six strong EASM-indicated principal components (explaining 70.21% of variations of all the strong EASM-indicated proxies input) and four weak EASM-indicated principal components (explaining 78.11% of the variations of all the weak EASM-indicated proxies input) (Table 4). Total principal factor scores (strong/weak EASM

Table 3. RDA classification results of paleoclimatic proxy taxa in peatlands, Northeastern China.

Proxy function	Proxy	Taxa
Strong EASM-indicated	Phytolith	Bilobate, cylindrical polylobate, cross, bulliform, saddle, blocky <i>Pinus</i> , <i>Alnus</i> , <i>Betula</i> , <i>Ulmus</i> , <i>Quercus</i> , <i>Corylus</i> , <i>Ephedra</i> , <i>Carpinus</i> , <i>Tilia</i> , <i>Acer</i> , <i>Juglans</i> , Poaceae, Chenopodiaceae, Trees, broad-leaved tree, shrub
	Pollen	
Weak EASM-indicated	Grain size	LOI, Mz, sand, >37 μm
	Phytolith	Elongate, lanceolate, trapeziform crenate, rondel, square, <i>Picea</i> , <i>Abies</i> , <i>Larix</i> , <i>Artemisia</i> , Cyperaceae, Asteraceae, Conifer, herbs
	Pollen	
	Grain size	
		Silt, clay, <37 μm

Table 4. Eigen values and the weights for each principal component obtained from PCA for the Hani peat proxies.

ID	Proxy function	Principal component	Eigen value	Variation explained (%)	Cumulative variation explained (%)
Hani	Strong EASM-indicated	PC1	5.77	26.25	26.25
		PC2	3.17	14.43	40.68
		PC3	2.57	11.66	52.34
		PC4	1.52	6.91	59.25
		PC5	1.29	5.87	65.12
		PC6	1.12	5.09	70.21
	Weak EASM-indicated	PC1	5.62	37.46	37.46
		PC2	3.01	20.06	57.52
		PC3	1.65	11.01	68.53
		PC4	1.44	9.59	78.11

scores) were calculated as the sum of weighted scores for each principal component. Higher values of the total principal factor scores represented stronger/weaker monsoon climate respectively; the composite climate indices (CCI) were calculated as the sum of the strong EASM scores and weak EASM scores. According to the definition, the greater values of the CCI indicated a stronger EASM phase in the study region (Figure 5).

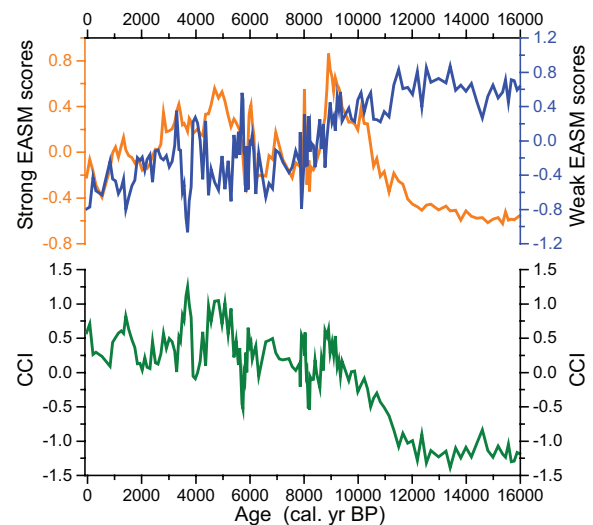
Wavelet and spectral analysis results

The complete ensemble empirical mode decomposition (CEEMD) of the Hani CCI series identified four major components (Table S2, Figure 6) with different frequencies centered at 500, 1100, 1875, and 4730 years (Figure 6a–d). Considering the length of the Hani CCI record (~11,700 year), the 4730-year periodicity should be treated with caution and is therefore not included in further discussion. REDFIT analysis results showed that multiple statistically significant periodicities (identified by the Monte-Carlo test) are recorded in the pollen-spore, phytolith, and grain size-derived CCI (Figure 7f). Statistically significant periodicities of *ca.* 1075, 600, 475, 350, 300 years were identified in the spectrum of Hani CCI sequences.

Discussion

Millennial and centennial climate cycles registered in Holocene paleoclimate reconstructions in northern and northeastern China

Holocene millennial climate cycles. Numerous periodicities have been detected in Holocene paleoclimate records in monsoonal China (e.g. Hong et al., 2000; Liu et al., 2012; Stebich et al., 2015; Wu et al., 2019; Xu et al., 2014, 2019). However, the robustness of many of these periodicities has been questioned since they are highly dependent on the individual age-depth models and may be affected by the data-sampling resolution (Swindles et al., 2007). CEEMD and wavelet analyses showed that the Hani CCI profile is paced by a ~1800-year

**Figure 5.** Strong EASM scores (in orange), weak EASM scores (in blue) and composite climate index (CCI) calculations (in green) for Hani peatland.

(1875-year) rhythm (Component 3). The strong EASM phases occurred at around 9100–8800, 8000–7700, 6800–6500, 5300–5000, 3600–3400, 1600–1200 cal. yr BP, whereas several weak-EASM phases peaked at around 8400–8100, 7400–7200, 5900–5600, 4300–4100 cal. yr BP (Figure 6). Some of these weak-EASM peaks coincided with Bond cycles, implying a possible tele-connection between monsoon climate and global oceanic oscillations.

Hani CCI records exhibit a clear cyclic oscillation signal at 1000-year periodicity (Figures 6 and 7f), which has been detected in past solar activity reconstructions (Liu et al., 2012; Steinhilber et al., 2012; Stuiver and Braziunas, 1993). Using cosmic nuclides production rates, solar variability is suggested to be characterized by a ~1000-year intrinsic

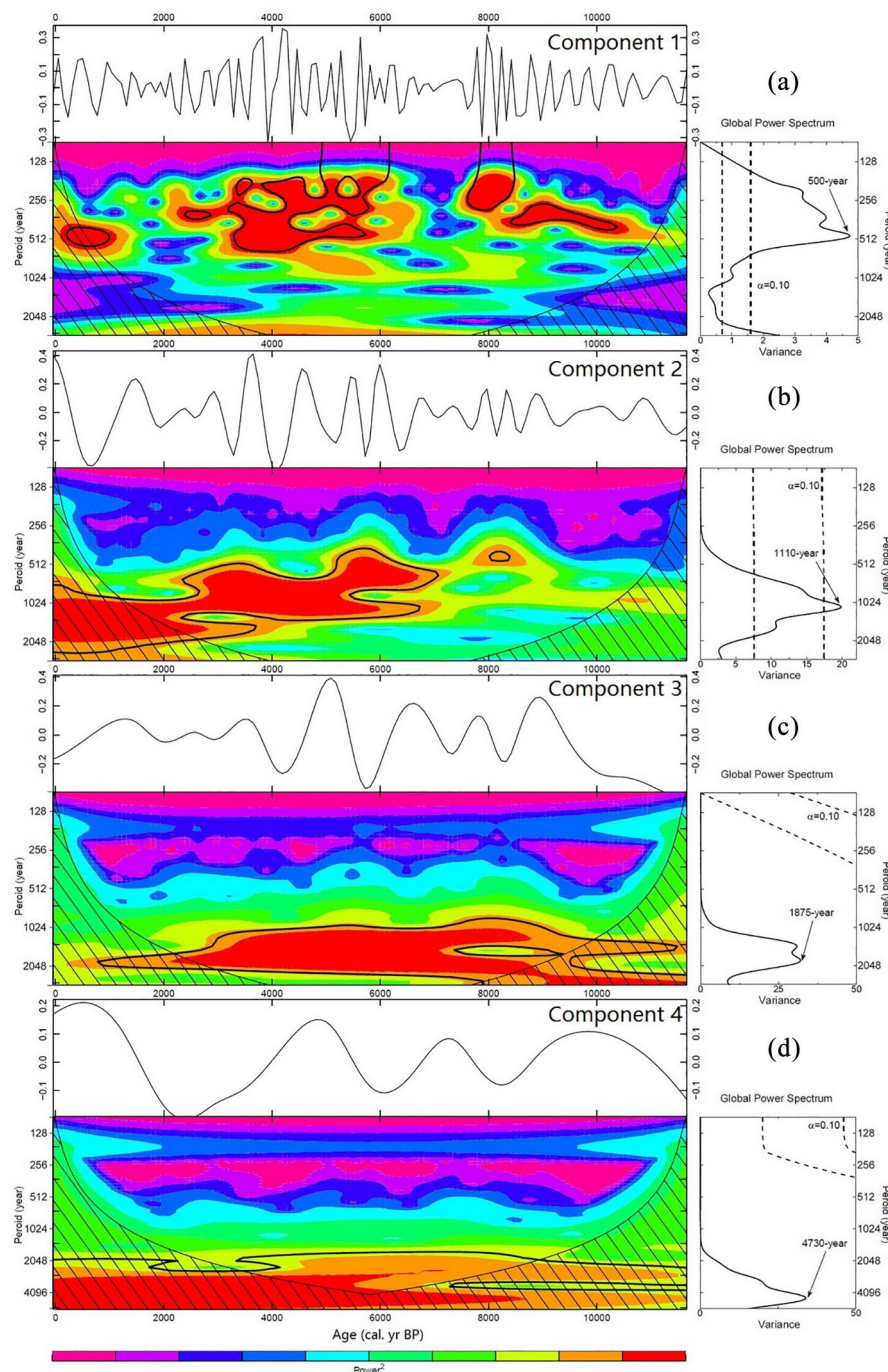


Figure 6. Wavelet power spectrum of the major components of Hani CCI time series using the Morlet wavelet (Torrence and Compo, 1998) and complete ensemble empirical mode decomposition (CEEMD) approach (Torres et al., 2011). (a) Component 1: 500-year periodicity. (b) Component 2: 1110-year periodicity. (c) Component 3: 1875-year periodicity. (d) Component 4: 4730-year periodicity. The black shade zone denotes the cone of influence, and black boundaries mark 1σ confidence level. The color bar refers to the wavelet power values from purple (low values), to red (high values). The global power spectrum with the most significant peaks of spectral power is shown on the right panel.

oscillation, known as “Eddy cycles” (Liu et al., 2012; Steinhilber et al., 2012). This ~ 1000 -year cycle has been identified in various paleoclimate records globally (e.g. Chu et al., 2014; Hong et al., 2000; Jo et al., 2017; Liu et al., 2019; Stuiver and Braziunas, 1993). For example, “Eddy cycles” have been reported in the $\delta^{18}\text{O}$ sequences of the GISP2 ice-core record from Greenland (Stuiver et al., 1995), Iceland Scotland Overflow water (ISOW, Bianchi and McCave, 1999) and the marine sedimentary lightness records from North Atlantic deep water (NADW) circulation (Chapman and Shackleton, 2000). Records from Southern Siberia revealed that, even in the far interior, the sun paced the

variations of climate changes there, displaying a significant ~ 1000 -year cycle (Kravchinsky et al., 2013).

In the present study, the approximately 1000-year (910-year) cycle registered in Hani CCI (Figure 7f) and the Holocene *Pinus* profile of Lake Moon (Figure 7a), which may correspond to the ~ 1000 -year cycle that has been well-documented in lacustrine sediments (e.g. Liu et al., 2000; Zhang et al., 2018), peatlands (e.g. Hong et al., 2000; Yu et al., 2008) and stalagmite records (Jo et al., 2017; Wang et al., 2005a), suggests possible solar-paced monsoon cyclic variations for this area. The discovery of the *ca.* 1000-year cycle may suggest that solar forcing has governed the Holocene paleoclimatic and paleoenvironmental fluctuations in northeastern Asia.

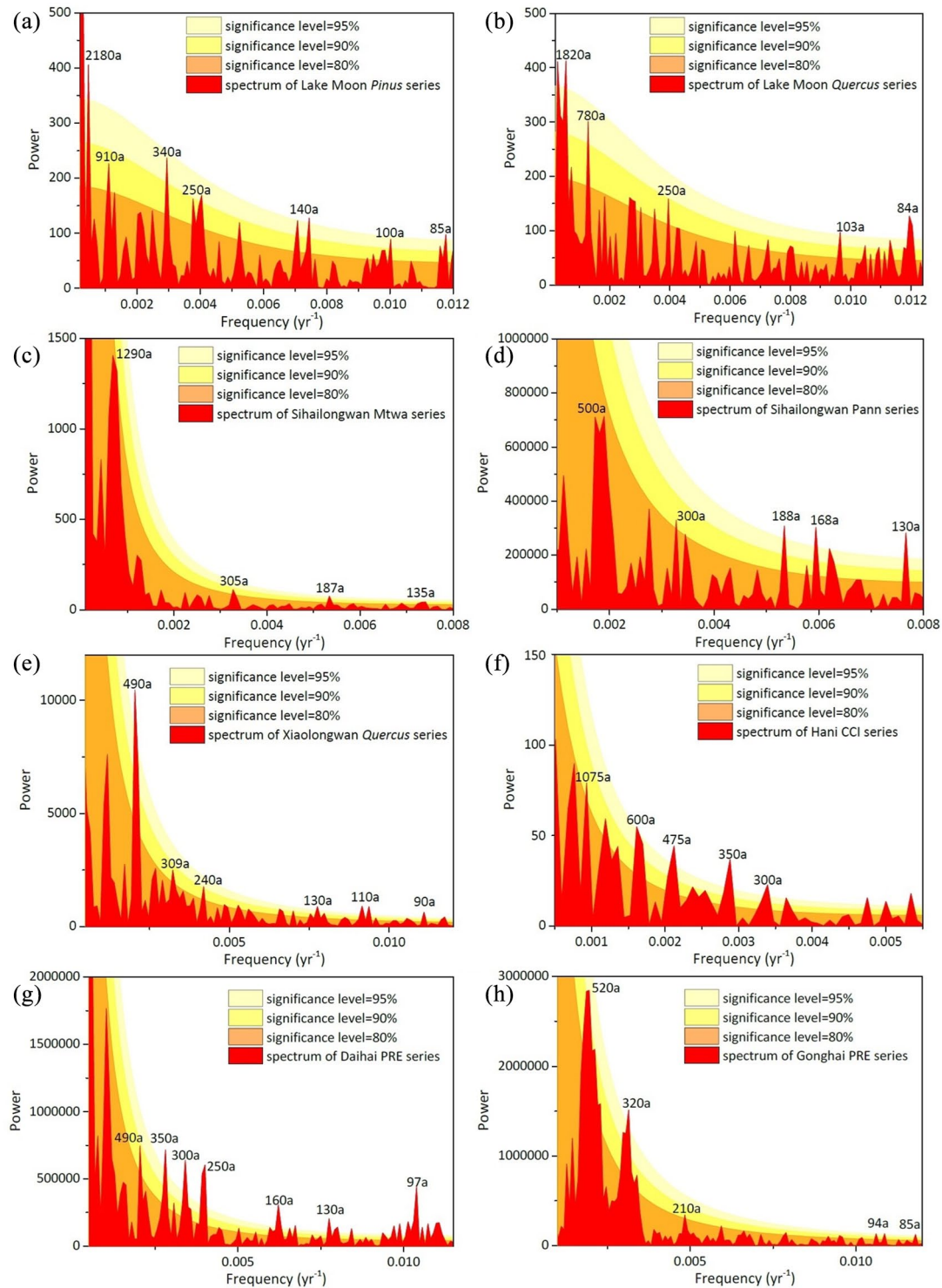


Figure 7. Spectral analysis of Holocene paleoclimate/paleovegetation records in East Asia. (a) *Pinus* pollen contents in Lake Moon (Wu et al., 2019). (b) *Quercus* pollen contents in Lake Moon (Wu et al., 2019). (c) Pollen-reconstructed July temperature (Mtw) from Lake Sihailongwan (Stebich et al., 2015). (d) Pollen-reconstructed mean annual precipitation (Pann) from Lake Sihailongwan (Stebich et al., 2015). (e) *Quercus* pollen percentages in Lake Xiaolongwan (Xu et al., 2019). (f) Hani CCI profile (this study). (g) pollen-reconstructed mean annual precipitation (Pann) from Lake Daihai (Ding et al., 2018; Xiao et al., 2004). (h) Pollen-reconstructed mean annual precipitation (Pann) from Lake Gonghai (Ding et al., 2018; Xu et al., 2017).

Upper Light yellow, yellow, and orange areas denote 95%, 90% and 80% confidence of periodicity by Monte-Carlo Test relative to an ARI background, respectively; power spectra calculated using the REDFIG 3.8e (Schulz and Mudelsee, 2002).

Holocene centennial climate cycles. The 475-year and 600-year cycles detected in Hani CCI sequences correspond well with the 550–600 years period that was previously reported from Lake Sihailongwan, which is only 10 km away from the Hani peatland (Stebich et al., 2015). The 500-year cycle has also been reported by Xu et al. (2014, 2019, 2020) from the pollen-spore records in

Lake Xiaolongwan (16 km away from Hani peatlands), and from stable oxygen isotopes of peat α -cellulose from Jinchuan bog (20 km away from Hani peatlands, Hong et al., 2000).

CEEMD processing identified several ~500-year cyclical components (Figure 8) from the mean July temperature, mean annual precipitation reconstructions, and *Quercus* pollen percentages from

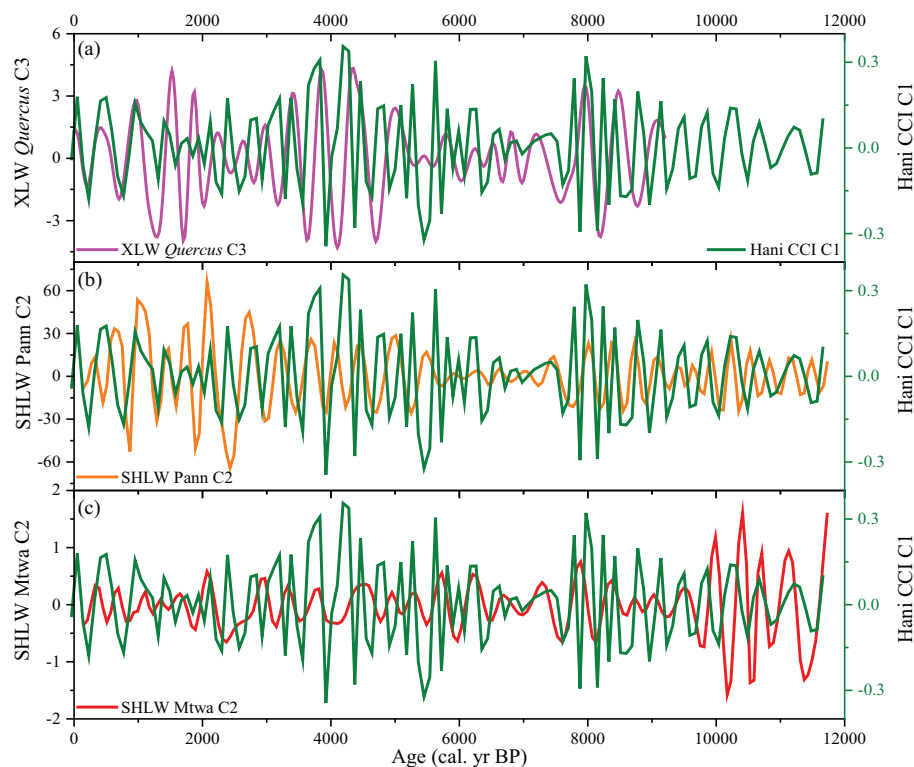


Figure 8. 500-year components extracted from different paleoclimate/paleovegetation sequences and their comparison with Hani CCI component 1 (green line). (a) *Quercus* pollen profile from Lake Xiaolongwan (Xu et al., 2019) versus Hani CCI. (b) Pollen-reconstructed mean annual precipitation (Pann) from Lake Sihailongwan (Stebich et al., 2015) versus Hani CCI. (c) Pollen-reconstructed July temperature (Mtw) from Lake Sihailongwan (Stebich et al., 2015) versus Hani CCI.

the nearby records (Stebich et al., 2015; Xu et al., 2019). Those ~500-year components, which were extracted from different cores with independent chronologies, almost co-varied in-phase with component 1 (at ~500-year frequency) of the Hani CCI sequence (Figure 8), indicating that the ~500-year cycle is not produced by site-specific effects or chronological differences. Instead, the ~500-year periodicity is persistent in nature and exists in Holocene paleoclimate sequences over an extensive region. The *ca.* 500-year periodicity is not limited to monsoonal Asia (e.g. Cosford et al., 2008; Dykoski et al., 2005; Liu et al., 2014b) but has also been registered in peats (e.g. Blundell and Barber, 2005; Sharifi et al., 2015; Swindles et al., 2007, 2012), marine (Patterson et al., 2004), lacustrine (Hu et al., 2003), and speleothem records (Springer et al., 2008) from other bioclimatic zones globally. Considering the existence of inherent 512- and 550-year cycles in high-resolution tree ring $\Delta^{14}\text{C}$ records (Stuiver and Braziunas, 1993; Stuiver et al., 1995), the detection of the ~500-year cycle in the Hani CCI profile and other paleoclimate sequences may suggest the role of the sun in regulating monsoonal climate variations at this frequency.

The 300–350-year periodicity exists in the spectra of all analyzed paleoclimate sequences (Figure 7) and has been found in various paleoclimate reconstructions using different geological archives (e.g. Hong et al., 2000; Ji et al., 2005; Jo et al., 2017; Li et al., 2016; Yu et al., 2008). Although evidence for the existence of *ca.* 300-year cycle is increasing (e.g. Chapman and Shackleton, 2000; Hong et al., 2000; Ji et al., 2005; Jo et al., 2017; Li et al., 2016), few studies demonstrated the possible forcing of periodic climate oscillations at this frequency. In addition to ~210-year (“de Vries cycle”) and ~1000-year (“Eddy cycle”) periodicities, wavelet analysis of cosmic-isotope-based Holocene solar activities have detected an unnamed significant cycle at about 350-year (e.g. Steinhilber et al., 2012), underscoring a possible inherent oscillation of solar irradiation. The significant 300–350-year periodicity detected in Hani CCI and other paleoclimate profiles (Ding et al., 2018; Stebich et al., 2015; Wu et al., 2019; Xu et al.,

2019) may therefore indicate a link between East Asian monsoon climate and solar irradiation (Steinhilber et al., 2012).

The ~200-year periodicity was found in various paleoclimate records in East Asia (Figure 7). Globally, the ~200-year periodicity has been identified in a range of paleoenvironmental records (Chambers et al., 1999), including peats (Aaby, 1976; Borgmark, 2005; Chambers and Blackford, 2001; Hong et al., 2000; Sharifi et al., 2015; Spiridonov et al., 2019) and lacustrine sediments (Cooper et al., 2000; Liu et al., 2000), and marine records (Kunzendorf and Larsen, 2002; Patterson et al., 2007). It is one of the most well-known unambiguous solar-related periodicities, not only because numerous publications show its existence in various records, but also it is registered in past solar reconstructions and historic solar activity monitoring (e.g. Stuiver and Braziunas, 1993). For instance, using historical “naked-eye” observations of sunspots between 165 BCE and 1918 CE, Vaquero et al. (2002) reported a persistent ~250-year cycle. Wagner et al. (2001) also reported a 205-year cycle is persistent in GRIP ice ^{10}Be sequences. In addition, a similar 208-year period was found in tree ring $\Delta^{14}\text{C}$ sequences (Stuiver and Braziunas, 1993).

In summary, the detection of millennial and centennial climate cycles from the Holocene Hani CCI profile and the consistency between different records demonstrates that the periodic oscillation of Holocene climate at different frequencies is persistent over an extensive region in East Asia. Although our records are from a single core, the multi-proxy based CCI data of the Hani core can be treated as a representative investigation in northeastern China.

Role of the sun in regulating East Asian monsoon climate and its possible mechanism

Linkage between solar irradiation and Holocene monsoon climate change. Wavelet and spectral analyses showed that the ~1875-year, ~1100-year, ~500-year, and 350-year periodicities characterize the Hani CCI profile (Figures 6 and 7). Among

these, the *ca.*1000-year, 500-year, 350-year periodicities correspond to \sim 1000-year (Eddy cycle), \sim 500-year, and \sim 350-year cycles that relate to solar activity (Steinhilber et al., 2012; Stuiver and Braziunas, 1993; Vaquero et al., 2002; Wagner et al., 2001). Cross-wavelet coherency analysis shows that the Hani CCI component 1 (at 500-year frequency) displayed a clear in-phase variation with corresponding cyclic components extracted from tree ring $\Delta^{14}\text{C}$ profiles (Reimer et al., 2013), especially at the frequency of 350–500-year (Figure 9). The CCI component 1 at 500-year peaked when there is a corresponding peak in the reconstructed solar activity (Figure 9a). A slight discrepancy, however, exists in the timing and amplitude of the CCI components relative to the $\Delta^{14}\text{C}$ fluctuations (Figure 9). Uncertainties in the chronological modeling of the peat core is probably the main reason for this discrepancy. Generally, however, based on the current chronology, the CCI components variations at 500-year and 1000-year matched well with $\Delta^{14}\text{C}$ inferred solar activity (Figure 9).

Unlike the other periodicities, the origin of the \sim 1800-year cycle and its external forcing is still disputed (e.g. Debret et al., 2007; Soon et al., 2014). According to Debret et al. (2007), the \sim 1800-year cycle was reported to be mainly related to internal oceanic oscillations, rather than solar forcing, which is characterized by *ca.* 1000-year, 500-year, 200-year and 11-year cycles (Soon et al., 2014). However, employing wavelet transform analysis, Soon et al. (2014) detected novel 1500-year and 1800-year cycles in solar activity proxy datasets. The 1500–1800-year cycle was captured by three different solar proxies (Nitrate concentration from TALDICE ice core (Traversi et al., 2012); solar modulation parameter Φ derived from ^{10}Be of GRIP (Steinhilber et al., 2009); ^{14}C production rates (Stuiver and Braziunas, 1993)). Since all these proxies show a similar relation to solar activity, and since each has a quite different destiny in the terrestrial system, the results may imply solar activity could be responsible for the 1500- to 1800-year climatic variations in paleo-records (Soon et al., 2014) and in solar dynamo modeling (Pipin et al., 2012). Therefore, it is unwise to reject the possibility that the \sim 1800-year cycle in the Hani CCI sequence may be connected to intrinsic variations in solar irradiation output.

A conceptual model for solar-triggered monsoon climate variability in East Asia. Eastern China is deeply influenced by the monsoon climate, which is affected by land-sea contrast, sea surface temperatures, and inter-hemispheric heat gradients (Chao and Chen, 2001; Wang et al., 2005b). Located between the world's largest continent (Eurasia) and ocean (Pacific), the East Asian monsoon is characterized by a moist southeasterly summer monsoon and a strong northwesterly (and/or northeasterly) winter monsoon (Wang et al., 2005b). Owing to the difference in heat capacity between the ocean and the continent, the EASM intensity is controlled by the ocean-land air pressure gradient, which can be further influenced by variations in solar irradiation (Beck et al., 2018). During high solar irradiation periods (boreal summer-like scenario), a large ocean/continent air pressure gradient and the northward movement of the Intertropical Convergence Zone (ITCZ), accompanied by heating over the Tibetan Plateau, strongly enhances the Asian monsoon (Chao and Chen, 2001; Wang et al., 2017). The strengthened EASM brings more precipitation to northern and northeastern China during the growing season, and this favors the growth of trees and also results in increased surface erosion in the lake (peatland) basin. It is therefore reasonable to deduce that more tree pollen and warmth-indicated phytoliths, as well as coarser grains, are recorded in the Hani peatland.

However, it should be noted that the change in total solar irradiance (ΔTSI) is less than $2\text{w}\cdot\text{m}^{-2}$ over the past 9300 years (Steinhilber et al., 2009). A simultaneous amplifying mechanism

is needed to produce the bigger climatic variations observed in paleoenvironmental reconstructions (e.g. Beck et al., 2018; Kravchinsky et al., 2013). El Niño–Southern Oscillation (ENSO) is a leading source of inter-annual climate variability over large regions of the globe (Ruzmaikin, 1999; Xie et al., 2009). It balances the water vapor transport and atmospheric circulation via feedbacks between surface wind and sea surface temperature (SST) distributions in the eastern and western Pacific. Increasing evidence indicates that slight changes in solar irradiation can be amplified via El Niño/La Niña (e.g. Liu et al., 2019; Lu et al., 2019; Rao et al., 2016). For example, employing stochastic resonance theory, Ruzmaikin (1999) suggested that the 11-year variation of solar forcing, although weak, can be effectively amplified through a nonlinear system when its period is close to twice that of the noise (Gammaitoni et al., 1998). White and Liu (2008) suggested that internal non-linear processes in the solar-forced Pacific delayed action/recharge oscillator (DAO) drove the \sim 3.6-year (one-third of \sim 11-year cycle) and \sim 2.2-year (one-fifth of \sim 11-year cycle) ENSO signals, indicating a feedback between the solar forcing and ENSO phases. In the present study, Hani CCI sequences show a general anti-phase variation with the TRACE simulated ENSO variabilities at the millennial scale (Figure 10). The proxy-based Hani CCI is more likely to drop during a strengthened ENSO phase, namely “El Niño”-like pattern (Figure 10). However, when the ENSO activity weakens (a “La Niña”-like pattern), the Hani CCI is more likely to increase (Figure 10). Based on modern observations and climate modeling (Chao and Chen, 2001; Ding et al., 2008; Lu et al., 2019; Rao et al., 2016; Xie et al., 2009), we propose a conceptual model to illustrate the influence of solar activity and ENSO variations on East Asian monsoon variabilities (Figure 11).

During high solar irradiation phases (Figure 11a), the northward migration of the ITCZ enhances the trade wind significantly (Chao and Chen, 2001; Wang et al., 2005b). The enhanced trade winds blow surface sea water to the western Pacific (Beck et al., 2018), forming a La Niña like phase (Figure 11c). As a result, the western Pacific sea surface temperature (SST) increases and stores a large amount of heat in the Western Pacific Warm Pool (WPWP) (Xu et al., 2013). The persistent warming in the western Pacific induces northeasterly winds and divergence north of the equator (Xie et al., 2009). The Ekman divergence restrains deep convection over the Northwest Pacific, amplifying the surface high pressure, namely Northwest Pacific Subtropical High (NPSH) (Figure 11a). The strengthened southeasterly monsoonal wind increases moisture transport from the western Pacific to East Asia, causing increased precipitation in the subtropical monsoon frontal region (Ding et al., 2008; Fan et al., 2016; Lu et al., 2019; Xie et al., 2009), for example, north and northeastern China. The Yangtze River basin, which is under the control of NPSH, experiences a decrease in regional precipitation (Figure 11a). In short, the intensified NPSH increases the frontal precipitation in north and northeastern China, but it causes a decrease in precipitation and even droughts in the Yangtze River basin.

In contrast, in a diminished insolation period (Figure 11b), the decreased Walker circulation will weaken the surface sea water blowing to the western Pacific (Beck et al., 2018), causing an El Niño like phase in the Pacific (Figure 11d, Ding et al., 2008; Liu et al., 2019; Xie et al., 2009). The NPSH is not as strong/active as during a high insolation period (Figure 11b). The position and zone of influence of NPSH is limited to southern China (Ding et al., 2008; Xu et al., 2020). Thus, the Yangtze River basin is exposed to the control of frontal precipitation of NPSH, resulting in enhanced regional precipitation there, whereas northern and northeastern China experience a shortage of rainfall (Ding et al., 2008; Liu et al., 2019; Xie et al., 2009), corresponding to a scenario of a weakened monsoon intensity period (Ding et al., 2008; Liu et al., 2019; Rao et al., 2016).

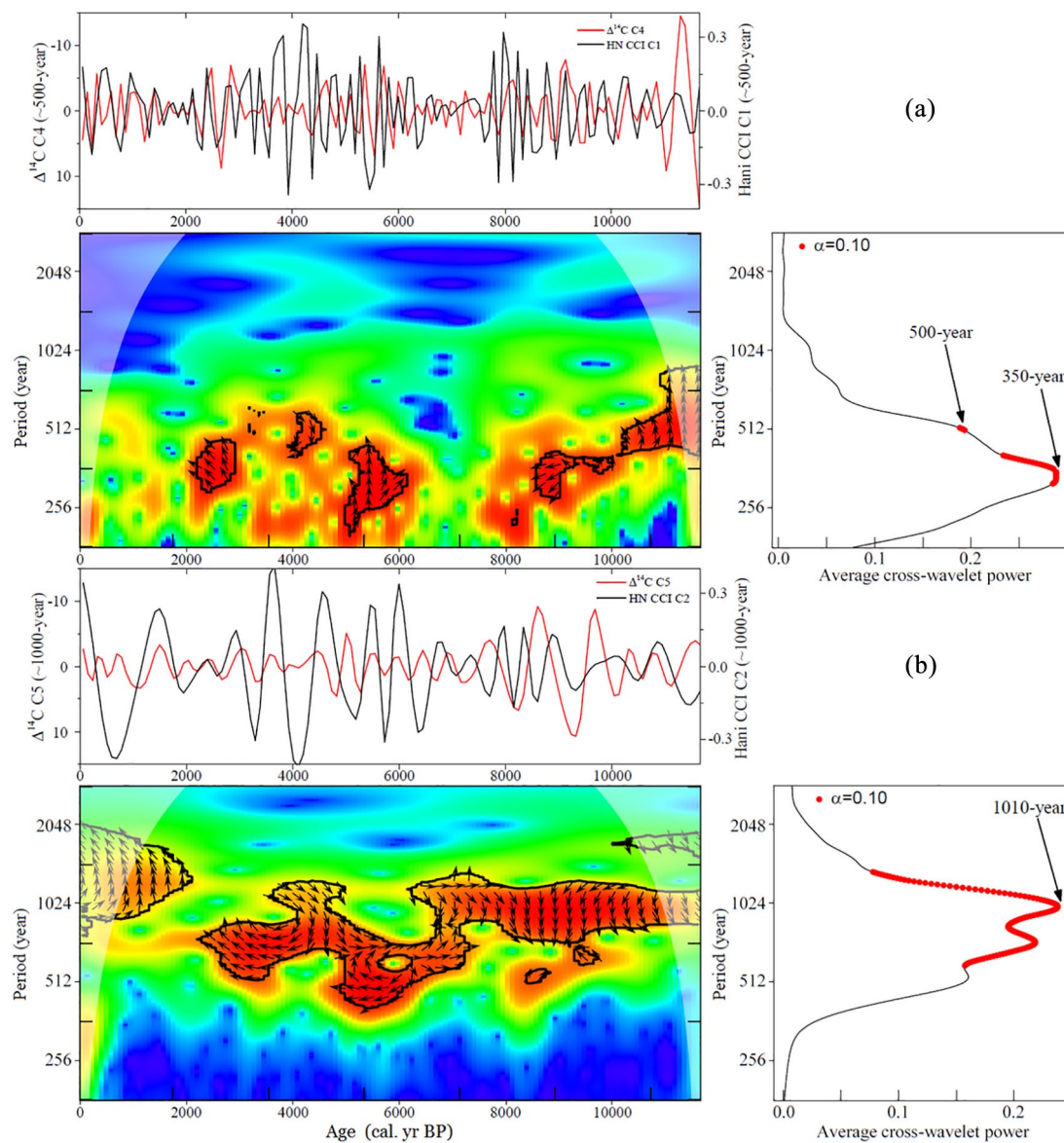


Figure 9. Cross wavelet coherence analysis between Hani CCI component 1 (500-year periodicity, a), component 2 (1000-year, b) and $\Delta^{14}\text{C}$ components at 500-year and 1000-year periodicities.

Phase arrows indicate the relative phase relationship of the time series (pointing right: in-phase; pointing left: anti-phase; and pointing straight down: leading by 90°). The thick black contour enclosed regions are greater than 90% confidence for a red-noise process. The white shade zone indicates the “cone of influence,” where edge effects become important.

These spatially opposite “wet (dry) north and dry (wet) south” phases have been recognized and confirmed via observations (e.g. Ding et al., 2008; Xu et al., 2020) and proxy-based reconstructions (e.g. Liu et al., 2019; Lu et al., 2019; Rao et al., 2016). Slight solar variation, associated with ocean-atmosphere feedbacks, is the most likely factor that regulates the East Asian monsoon climate change. In a higher solar activity period, the intensified summer monsoon across eastern China is always accompanied by intensified rainfall in northern and northeastern China and by reduced rainfall over the Yangtze River basin. In contrast, during a diminished solar irradiation period, the weakened EASM climates across eastern China are characterized by a decrease of rainfall in northern and northeastern China and by increased rainfall in most of southern China.

Conclusions

Using peatland paleoecological data, a composite climatic index (CCI) was defined and calculated to investigate the periodic

oscillation features of Holocene climate in East Asia. Statistically significant *ca.* 1800-year, 1000-year, 500-year, and 350-year periodicities were detected in the Hani CCI time series and other Holocene paleoclimatic sequences in northern and northeastern China. Cross-wavelet coherency analysis showed the CEEMD extracted 500-year component displayed a clear in-phase variation with past solar activity, indicating a link between East Asian monsoonal climate and solar forcing. Given the in-phase variations between our records and solar activity reconstructions, and possible anti-phase variations between Hani CCI and simulated ENSO variabilities, it seems that variation in solar irradiation, associated with ENSO activity, is mainly responsible for these centennial- to millennial- climate cycles observed in paleo-records. Based on modern climate observations and numerical modeling, we propose a conceptual model to argue that the relationship between East Asian monsoon climate change and solar forcing involves sun-atmosphere-ocean interactions and regulations. Amplified by ocean-atmosphere feedbacks, slight solar insolation change could trigger significant climate variations in East Asia during the Holocene.

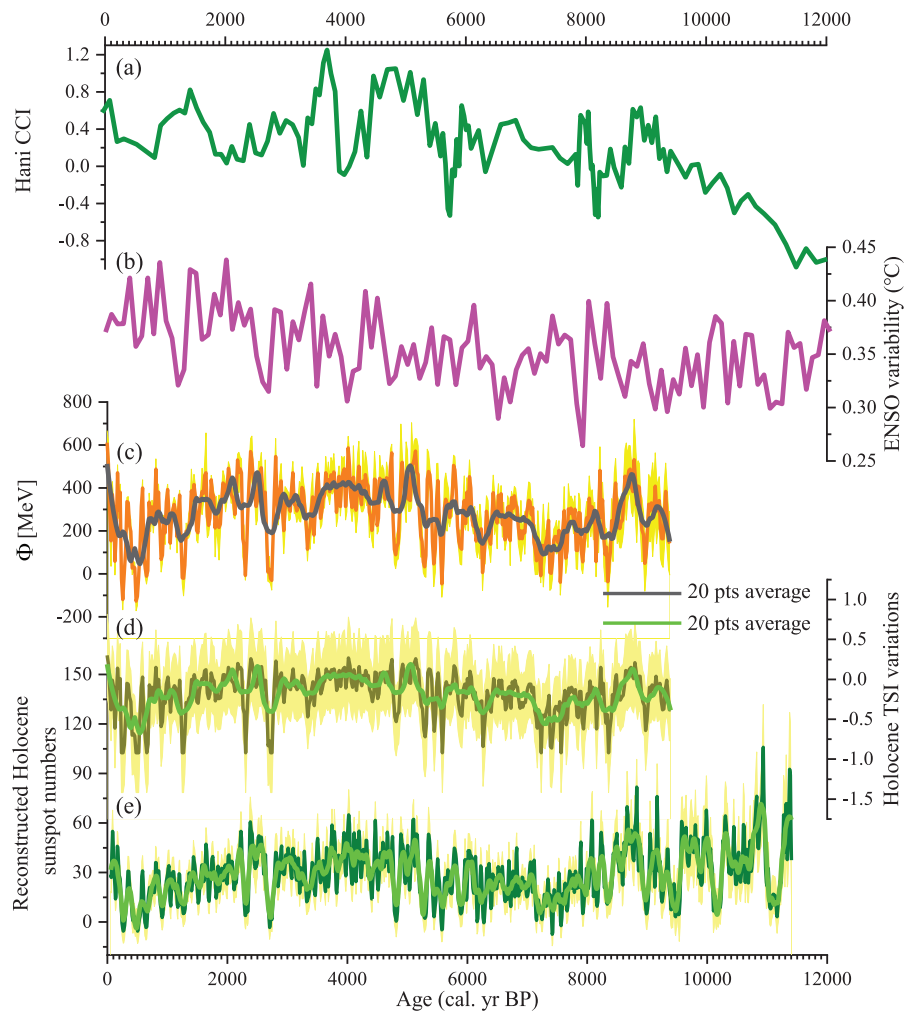


Figure 10. Comparisons of (a) Hani CCI records (this study) with (b) TRACE simulated ENSO variabilities (Liu et al., 2014a) and (c, d, e) past solar activity reconstructions (Solanki et al., 2004; Steinhilber et al., 2009, 2012).

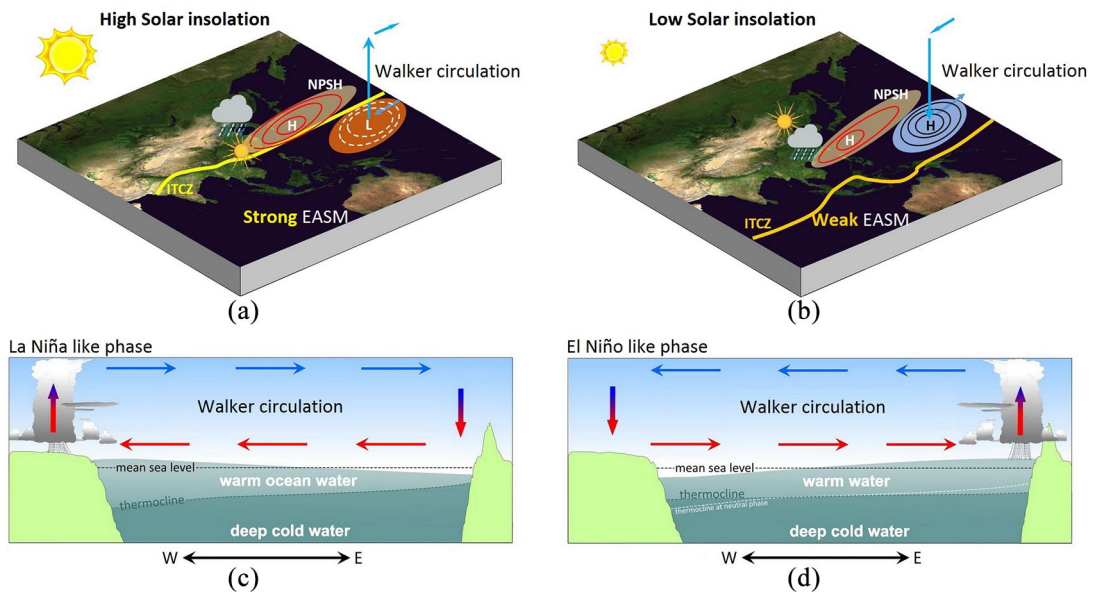


Figure 11. Sketch maps of Eastern Asia showing the spatial patterns of precipitation and related circulation characteristics under different solar insolation scenarios. During high solar insolation stages, migration of ITCZ and intensified trade winds enhanced the EASM, forming a “La Niña” like atmospheric and oceanic circulation pattern (c). This resulted in increased precipitation in northern and northeastern China but a decrease in rainfall in the Yangtze River basin (a). During low solar irradiation intervals, the opposite occurs (an “El Niño” like circulation pattern), as shown in (b) and (d), resulting in intensified rainfall in the Yangtze River basin, but a decrease in precipitation (even droughts) in northern and northeastern China.

Acknowledgements


We thank two anonymous reviewers for their insightful comments that greatly improved the manuscript. Dr. Zhengyao Lu (Lund University, Sweden) is acknowledged for kindly providing the TRACE simulated ENSO variability data.

Funding

The author(s) disclosed receipt of the following financial support for the research, authorship, and/or publication of this article: This work was financially supported by the National Natural Science Foundation of China (Grant No. 41771214, 41471164, and 41971100) and the National Key Research and Development Project of China (Grant No. 2016YFA0602301).

ORCID iDs

Nannan Li  <https://orcid.org/0000-0002-0993-6900>

Dongmei Jie  <https://orcid.org/0000-0003-2398-6127>

Supplemental material

Supplemental material for this article is available online.

References

- Aaby B (1976) Cyclic climatic variations in climate over past 5,500 yr reflected in raised bogs. *Nature* 263: 281–284.
- Amante C and Eakins BW (2009) *ETOPO1 1 Arc-Minute Global Relief Model: Procedures, Data Sources and Analysis*. NOAA Technical Memorandum NESDIS NGDC-24. National Geophysical Data Center, NOAA. DOI: 10.7289/V5C8276M.
- Barber KE and Langdon PG (2007) What drives the peat-based palaeoclimate record? A critical test using multi-proxy climate records from northern Britain. *Quaternary Science Reviews* 26: 3318–3327.
- Beck JW, Zhou W, Li C et al. (2018) A 550,000-year record of East Asian monsoon rainfall from ¹⁰Be in loess. *Science* 360: 877–881.
- Bianchi GG and McCave N (1999) Holocene periodicity in North Atlantic climate and deep-ocean flow south of Iceland. *Nature* 397: 515–517.
- Blaauw M and Christen JA (2011) Flexible paleoclimate age-depth models using an autoregressive gamma process. *Bayesian Analysis* 6: 457–474.
- Blundell A and Barber KE (2005) A 2800-year palaeoclimatic record from Tore Hill Moss, Strathspey, Scotland: The need for a multi-proxy approach to peat-based climate reconstructions. *Quaternary Science Reviews* 24: 1261–1277.
- Bond GC, Kromer B, Beer J et al. (2001) Persistent solar influence on North Atlantic climate during the Holocene. *Science* 294(5549): 2130–2136.
- Bond GC, Showers W, Cheseby M et al. (1997) A pervasive millennial-scale cycle in North Atlantic Holocene and glacial climates. *Science* 278(5341): 1257–1266.
- Borgmark A (2005) Holocene climate variability and periodicities in south-central Sweden, as interpreted from peat humification analysis. *The Holocene* 15: 387–395.
- Braun H, Christl M, Rahmstorf S et al. (2005) Possible solar origin of the 1470-year glacial climate cycle demonstrated in a coupled model. *Nature* 438(70695): 208–211.
- Cao X, Herzschuh U, Telford RJ et al. (2014) A modern pollen-climate dataset from China and Mongolia: Assessing its potential for climate reconstruction. *Review of Palaeobotany and Palynology* 211: 87–96.
- Chai X (1990) *Peatland*. Beijing: Geological Publishing House.
- Chambers FM and Blackford JJ (2001) Mid- and Late-Holocene climatic changes: A test of periodicity and solar forcing in proxy-climate data from blanket peat bogs. *Journal of Quaternary Science* 16: 329–338.
- Chambers FM, Booth RK, De Vleeschouwer F et al. (2012) Development and refinement of proxy-climate indicators from peats. *Quaternary International* 268: 21–33.
- Chambers FM and Charman DJ (2004) Holocene environmental change: Contributions from the peatland archive. *The Holocene* 14(1): 1–6.
- Chambers FM, Ogle MI and Blackford JJ (1999) Palaeoenvironmental evidence for solar forcing of Holocene climate: Linkages with solar science. *Progress in Physical Geography* 23: 181–204.
- Chao WC and Chen B (2001) The origin of monsoons. *Journal of the Atmospheric Sciences* 58: 3497–3507.
- Chapman MR and Shackleton N (2000) Evidence of 550-year and 1500-year cyclicities in North Atlantic circulation pattern during the Holocene. *The Holocene* 10: 287–291.
- Chen Y, Ni J and Herzschuh U (2010) Quantifying modern biomes based on surface pollen data in China. *Global and Planetary Change* 74: 114–131.
- Chen F, Xu Q, Chen J et al. (2015) East Asian summer monsoon precipitation variability since the last deglaciation. *Scientific Reports* 5: 11186, 1–11.
- Chu G, Sun Q, Xie M et al. (2014) Holocene cyclic climatic variations and the role of the Pacific Ocean as recorded in varved sediments from northeastern China. *Quaternary Science Reviews* 15: 85–95.
- Cooper MC, O'Sullivan PE and Shine AJ (2000) Climate and solar variability recorded in Holocene laminated sediments: a preliminary assessment. *Quaternary International* 68: 363–371.
- Cosford J, Qing H, Eglington B et al. (2008) East Asian monsoon variability since the Mid-Holocene recorded in a high-resolution, absolute-dated aragonite speleothem from eastern China. *Earth and Planetary Science Letters* 275: 296–307.
- Dansgaard W, Johnsen SJ, Clausen HB et al. (1993) Evidence for general instability of past climate from a 250-kyr ice-core record. *Nature* 364: 218–220.
- Darby DA, Ortiz JD, Grosch CE et al. (2012) 1,500-year cycle in the Arctic oscillation identified in Holocene Arctic sea-ice drift. *Nature Geoscience* 5: 897–900.
- Debret M, Bout-Roumzeilles V, Grousset F et al. (2007) The origin of the 1500-year climate cycles in Holocene North-Atlantic records. *Climate of the Past* 3: 569–575.
- Ding Y, Wang Z and Sun Y (2008) Inter-decadal variation of the summer precipitation in East China and its association with decreasing Asian summer monsoon. Part I: Observed evidences. *International Journal of Climatology* 28: 1139–1161.
- Ding W, Xu Q, Fu T et al. (2018) Heterogeneous vegetation sensitivity at local and regional scales: Implications for pollen-based climate reconstruction. *Quaternary International* 516: 149–159.
- Dise NB (2009) Peatland response to global change. *Science* 326: 810–811.
- Dykoski CA, Edwards RL, Cheng H et al. (2005) A high-resolution, absolute-dated Holocene and deglacial Asian monsoon records from Dongge cave, China. *Earth and Planetary Science Letters* 233: 71–86.
- Fan L, Shin SI, Liu Z et al. (2016) Sensitivity of Asian summer monsoon precipitation to tropical sea surface temperature anomalies. *Climate Dynamics* 47: 2501–2514.
- Gammaitoni L, Hänggi P, Jung P et al. (1998) Stochastic resonance. *Reviews of Modern Physics* 70: 223–287.
- Gao G, Jie D, Wang Y et al. (2018) Phytolith reference study for identifying vegetation changes in the forest-grassland region of Northeast China. *Boreas* 47: 481–497.
- Hong Y, Jiang H, Liu T et al. (2000) Response of climate to solar forcing recorded in a 6000-year $\delta^{18}\text{O}$ time-series of Chinese peat cellulose. *The Holocene* 10: 1–7.

- Hu FS, Kaufman D, Yoneji S et al. (2003) Cyclic variation and solar forcing of Holocene climate in the Alaskan subarctic. *Science* 301: 1890–1893.
- Huang C, Zeng T, Ye F et al. (2019) Solar-forcing-induced spatial synchronisation of the East Asian summer monsoon on centennial timescales. *Palaeogeography Palaeoclimatology Palaeoecology* 514: 536–549.
- Ji J, Shen J, Balsam W et al. (2005) Asian monsoon oscillations in the northeastern Qinghai–Tibet Plateau since the late glacial as interpreted from visible reflectance of Qinghai Lake sediments. *Earth and Planetary Science Letters* 233: 61–70.
- Jian Z, Wang P, Saito Y et al. (2000) Holocene variability of the Kuroshio Current in the Okinawa Trough, Northwestern Pacific Ocean. *Earth and Planetary Science Letters* 184: 305–319.
- Jo K, Yi S, Lee J-Y et al. (2017) 1000-Year quasi-periodicity of weak monsoon events in temperate Northeast Asia since the Mid-Holocene. *Scientific Reports* 7: 15196.
- Kravchinsky VA, Langereis CG, Walker SD et al. (2013) Discovery of Holocene millennial climate cycles in the Asian continental interior: Has the sun been governing the continental climate? *Global and Planetary Change* 110: 386–396.
- Kunzendorf H and Larsen B (2002) A 200–300 year cyclicity in sediment deposition in the Gotland Basin, Baltic Sea, as deduced from geochemical evidence. *Applied Geochemistry* 17: 29–38.
- Li N, Chambers FM, Yang J et al. (2017) Records of East Asian monsoon activities in Northeastern China since 15.6 ka, based on grain size analysis of peaty sediments in the Changbai Mountains. *Quaternary International* 447: 158–169.
- Li Y, Ma C, Zhou B et al. (2016) Environmental processes derived from peatland geochemistry since the last deglaciation in Dajiuhu, Shennongjia, Central China. *Boreas* 45(3): 423–438.
- Li N, Sack D, Sun J et al. (2020) Quantifying the carbon content of aeolian sediments: Which method should we use? *Catena* 185: 104276.
- Liu J (1988) The Cenozoic volcanic episodes in Northeast China. *Acta Petrologica Sinica* 4(1): 1–10 (in Chinese).
- Liu H, Gu Y, Huang X et al. (2019) A 13,000-year peatland palaeohydrological response to the ENSO-related Asian monsoon precipitation changes in the middle Yangtze Valley. *Quaternary Science Reviews* 212: 80–91.
- Liu H, Lin Z, Qi X et al. (2012) Possible link between Holocene East Asian monsoon and solar activity obtained from the EMD method. *Nonlinear Processes in Geophysics* 19: 421–430.
- Liu J, Lu H, Negendank J et al. (2000) Periodicity of Holocene climatic variations in the Huguangyan Maar Lake. *Chinese Science Bulletin* 45: 1712–1717.
- Liu Z, Lu Z, Wen X et al. (2014a) Evolution and forcing mechanisms of El Niño over the past 21,000 years. *Nature* 515: 550–553.
- Liu Z, Wen X, Brady EC et al. (2014b) Chinese cave records and the East Asia summer monsoon. *Quaternary Science Reviews* 83: 115–128.
- Lu F, Ma C, Zhu C et al. (2019) Variability of East Asian summer monsoon precipitation during the Holocene and possible forcing mechanisms. *Climate Dynamics* 52: 969–989.
- Lu H, Wu N, Yang X et al. (2006) Phytoliths as quantitative indicators for the reconstruction of past environmental conditions in China I: Phytolith-based transfer functions. *Quaternary Science Reviews* 25: 945–959.
- Luo Y and Sun X (2005) Vegetation evolution and millennial-scale climatic fluctuations since last glacial maximum in pollen record from northern South China Sea. *Chinese Science Bulletin* 50: 793–799.
- Obrochta SP, Miyahara H, Yokoyama Y et al. (2012) A re-examination of evidence for the North Atlantic “1500-year cycle” at Site 609. *Quaternary Science Reviews* 55: 23–33.
- Ojala AEK, Launonen I, Holmström L et al. (2015) Effects of solar forcing and North Atlantic oscillation on the climate of continental Scandinavia during the Holocene. *Quaternary Science Reviews* 112: 153–171.
- Patterson RT, Prokoph A and Chang C (2004) Late Holocene sedimentary response to solar and cosmic ray activity influenced climate variability in the NE Pacific. *Sedimentary Geology* 172: 67–84.
- Patterson RT, Prokoph A, Reinhardt E et al. (2007) Climate cyclicity in late Holocene anoxic marine sediments from the Seymour-Belize inlet complex, British Columbia. *Marine Geology* 242: 123–140.
- Piotrowska N, Blaauw M, Mauquoy D et al. (2011) Constructing deposition chronologies for peat deposits using radiocarbon dating. *Mires and Peat* 7: 10, 1–14.
- Pipin VV, Sokoloff DD and Usoskin IG (2012) Variations of the solar cycle profile in a solar dynamo with fluctuating dynamo governing parameters. *Astronomy and Astrophysics* 542: A26.
- Qiao S (1993) A preliminary study on Hani peat-mire in the west part of the Changbai Mountain. *Scientia Geographica Sinica* 13: 279–287 (in Chinese).
- Rao Z, Li Y, Zhang J et al. (2016) Investigating the long-term palaeoclimatic controls on the δD and $\delta^{18}O$ of precipitation during the Holocene in the Indian and East Asian monsoonal regions. *Earth-Science Reviews* 159: 292–305.
- Reimer PJ, Bard E, Bayliss A et al. (2013) IntCal13 and Marine13 radiocarbon age calibration curves 0–50,000 yr cal BP. *Radiocarbon* 55(4): 1869–1887.
- Reimer PJ, Austin WEN, Bard E et al. (2020) The IntCal20 Northern hemisphere radiocarbon age calibration curve (0–55 cal kBP). *Radiocarbon* 62(4): 725–757.
- Ruzmaikin A (1999) Can El Niño amplify the solar forcing of climate? *Geophysical Research Letters* 26: 2255–2258.
- Schulz M and Mudelsee M (2002) REDFIT: Estimating red-noise spectra directly from unevenly spaced paleoclimatic time series. *Computational Geosciences* 28: 421–426.
- Schröder C, Thiele A, Wang S et al. (2007) Hani-mire: A percolation mire in northeast China. *Peatlands International* 2: 21–24.
- Sharifi A, Pourmand A, Canuel EA et al. (2015) Abrupt climate variability since the last deglaciation based on a high-resolution, multi-proxy peat record from NW Iran: The hand that rocked the cradle of civilization? *Quaternary Science Reviews* 123: 215–230.
- Solanki SK, Usoskin IG, Kromer B et al. (2004) Unusual activity of the Sun during recent decades compared to the previous 11,000 years. *Nature* 431: 1084–1087.
- Soon W, Velasco Herrera VM, Selvaraj K et al. (2014) A review of Holocene solar-linked climatic variation on centennial to millennial timescales: Physical processes, interpretative frameworks and a new multiple cross-wavelet transform algorithm. *Earth-Science Reviews* 134: 1–15.
- Spiridonov A, Balakauskas L, Stankevič R et al. (2019) Holocene vegetation patterns in southern Lithuania indicate astronomical forcing on the millennial and centennial time scales. *Scientific Reports* 9: 14711.
- Springer GS, Rowe HD, Hardt B et al. (2008) Solar forcing of Holocene droughts in a stalagmite record from West Virginia in east-central North America. *Geophysical Research Letters* 35: L17703.
- Stebich M, Rehfeld K, Schlütz F et al. (2015) Holocene vegetation and climate dynamics of NE China based on the pollen record from Sihailongwan Maar Lake. *Quaternary Science Reviews* 124: 275–289.
- Steinhilber F, Abreu JA, Beer J et al. (2012) 9400 Years of cosmic radiation and solar activity from ice cores and tree rings. *Proceedings of the National Academy of Sciences of the United States of America* 109: 5967–5971.
- Steinhilber F, Beer J and Fröhlich C (2009) Total solar irradiance during the Holocene. *Geophysical Research Letters* 36: L19704.

- Stevens T, Buylaert JP, Thiel C et al. (2018) Ice-volume-forced erosion of the Chinese loess plateau global quaternary strato-type site. *Nature Communications* 9: 983, 1–12.
- Stuiver M and Braziunas TF (1993) Modeling atmospheric ^{14}C influence and ^{14}C ages of marine samples to 10,000 BC. *Radiocarbon* 35: 137–189.
- Stuiver M, Grootes P and Braziunas T (1995) The GISP2 $\delta^{18}\text{O}$ climate record of the past 16,500 years and the role of the sun, ocean, and volcanoes. *Quaternary Research* 44: 341–354.
- Stuiver M and Reimer PJ (1993) Extended ^{14}C database and revised CALIB radiocarbon calibration program. *Radiocarbon* 35: 215–230.
- Swindles GT, Patterson RT, Roe HM et al. (2012) Evaluating periodicities in peat-based climate proxy records. *Quaternary Science Reviews* 41: 94–103.
- Swindles GT, Plunkett G and Roe HM (2007) A multiproxy climate record from a raised bog in County Fermanagh, Northern Ireland: A critical examination of the link between bog surface wetness and solar variability. *Journal of Quaternary Science* 22: 667–679.
- ter Braak CJF and Šmilauer P (2002) *CANOCO Reference Manual and Canodraw for Windows User's Guide: Software for Canonical Community Ordination (Version 4.5)*. Ithaca, NY: Microcomputer Power.
- Torrence C and Compo GP (1998) A practical guide to wavelet analysis. *Bulletin of the American Meteorological Society* 79: 61–78.
- Torres E, Colominas MA, Schlotthauer G et al. (2011) A complete ensemble empirical mode decomposition with adaptive noise. In: *IEEE international conference on acoustics, speech and signal processing ICASSP-11, CFP11ICA-ART*, Prague, CZ, pp.4144–4147. Prague: IEEE.
- Traversi R, Usoskin IG, Solanki SK et al. (2012) Nitrate in polar ice: A new tracer of solar variability. *Solar Physics* 280: 237–254.
- Vaquero JM, Gallego MC and García JA (2002) A 250-year cycle in naked-eye observations of sunspots. *Geophysical Research Letters* 29(20): 1997.
- Wagner G, Beer J, Masarik J et al. (2001) Presence of the solar de Vries cycle (205 years) during the last ice age. *Geophysical Research Letters* 28: 303–306.
- Wang J (1989) *The Gazetteer of Changbai Mountains*. Changchun: Jilin Literature and History Press (in Chinese).
- Wang Y, Cheng H, Edwards RL et al. (2001) A high-resolution absolute-dated late pleistocene monsoon record from Hulu Cave, China. *Science* 294: 2345–2348.
- Wang Y, Cheng H, Edwards RL et al. (2005a) The Holocene Asian monsoon: Links to solar changes and North Atlantic climate. *Science* 308: 854–857.
- Wang P, Clemens S, Beaufort L et al. (2005b) Evolution and variability of the Asian monsoon system: State of the art and outstanding issues. *Quaternary Science Reviews* 24: 595–629.
- Wang W, Liu J and Zhou X (2003) Climate indexes of phytoliths from *Homo erectus*' cave deposits in Nanjing. *Chinese Science Bulletin* 48(18): 104–108.
- Wang Y and Lu H (1993) *The Study of Phytolith and Its Application*. Beijing: China Ocean Press, 228pp (in Chinese).
- Wang L, Sarntheim M, Erlenkeuser H et al. (1999) East Asian monsoon climate during the Late Pleistocene: High-resolution sediment records from the South China Sea. *Marine Geology* 156: 245–284.
- Wang P, Wang B, Cheng H et al. (2017) The global monsoon across time scales: Mechanisms and outstanding issues. *Earth-Science Reviews* 174: 84–121.
- Wanner H and Bütikofer J (2008) Holocene bond cycles: Real or imaginary? *Geografie* 113: 338–350.
- White WB and Liu Z (2008) Non-linear alignment of El Niño to the 11-yr solar cycle. *Geophysical Research Letters* 35: L19607.
- Wu Z (1980) *The Vegetation of China*. Beijing: Science Press (in Chinese).
- Wu J, Liu Q, Cui Q et al. (2019) Shrinkage of East Asia winter monsoon associated with increased ENSO events since the mid-Holocene. *Journal of Geophysical Research: Atmospheres* 124: 3839–3848.
- Xiao J, Xu Q, Nakamura T et al. (2004) Holocene vegetation variation in the Daihai Lake region of north-central China: A direct indication of the Asian monsoon climatic history. *Quaternary Science Reviews* 23: 1669–1679.
- Xie S-P, Hu K, Hafner J et al. (2009) Indian ocean capacitor effect on Indo-Western Pacific climate during the summer following El Niño. *Journal of Climate* 22: 730–747.
- Xu Q, Chen F, Zhang S et al. (2017) Vegetation succession and East Asian summer monsoon changes since the last deglaciation inferred from high-resolution pollen record in Gonghai lake, Shanxi province, China. *The Holocene* 27: 835–846.
- Xu D, Lu H, Chu G et al. (2014) 500-year climate cycles stacking of recent centennial warming documented in an East Asian pollen record. *Scientific Reports* 4: 3611, 1–7.
- Xu D, Lu H, Chu G et al. (2019) Synchronous 500-year oscillations of monsoon climate and human activity in Northeast Asia. *Nature Communications* 10: 4105.
- Xu D, Lu H, Chu G et al. (2020) Asynchronous 500-year summer monsoon rainfall cycles between Northeast and Central China during the Holocene. *Global and Planetary Change* 195: 103324.
- Xu D, Lu H, Wu N et al. (2013) Asynchronous marine-terrestrial signals of the last deglacial warming in East Asia associated with low- and high-latitude climate changes. *Proceedings of the National Academy of Sciences of the United States of America* 110: 9657–9662.
- Xu X, Trumbore SE, Zheng S et al. (2007) Modifying a sealed tube zinc reduction method for preparation of AMS graphite targets: Reducing background and attaining high precision. *Nuclear Instruments and Methods in Physics Research Section B* 259: 320–329.
- Yamada K, Kohara K, Ikehara M et al. (2019) The variations in the East Asian summer monsoon over the past 3 kyrs and the controlling factors. *Scientific Reports* 9: 5036.
- Yu G, Ke X, Xue B et al. (2004) The relationships between the surface arboreal pollen and the plants of the vegetation in China. *Review of Palaeobotany and Palynology* 129: 187–198.
- Yu C, Luo Y and Sun X (2008) A high-resolution pollen records from Ha'ni Lake, Jilin, Northeast China showing climate changes between 13.1 ka cal. BP and 4.5 ka cal. BP. *Quaternary Sciences* 28(5): 929–938 (in Chinese).
- Zhang M, Bu Z, Jiang M et al. (2019) The development of Hani peatland in the Changbai mountains (NE China) and its response to the variations of the East Asian summer monsoon. *Science of the Total Environment* 692: 818–832.
- Zhang Z, Huang W, Chen J et al. (2017) Multi-time scale analysis of East Asian summer monsoon and its possible mechanism during Holocene. *Quaternary Sciences* 37(3): 498–509 (in Chinese).
- Zhang W, Niu J, Ming Q et al. (2018) Holocene climatic fluctuations and periodic changes in the Asian southwest monsoon region. *Journal of Asian Earth Sciences* 156: 90–95.
- Zhu S, Ding P, Wang N et al. (2015) The compact AMS facility at Guangzhou institute of geochemistry, Chinese academy of sciences. *Nuclear Instruments and Methods in Physics Research Section B* 361: 72–75.
- Zhu Z, Feinberg JM, Xie S et al. (2017) Holocene ENSO-related cyclic storms recorded by magnetic minerals in speleothems of central China. *Proceedings of the National Academy of Sciences of the United States of America* 114(5): 852–857.